New insights in the 1963 Vajont slide using 2D and 3D Distinct Element Method analyses

C.W. Boon [a], G.T. Houlsby [a] and S. Utili [b]

[a] Department of Engineering Science, Parks Road, Oxford OX1 3PJ

[b] School of Engineering, University of Warwick, Coventry CV4 7AL, United Kingdom

Email: s.utili@warwick.ac.uk

Tel: (+44)24 765 22339

Abstract

The 1963 Vajont rock slide is studied using the distinct element method (DEM). 2-D and 3-D DEM models were constructed based on information published in the literature. In this study, a strength reduction approach was used to calculate the slide surface friction angles required for stability. The influence of several parameters was investigated in 2-D, namely the reservoir water level, the shear stiffness of the slide surface, the rock mass strength, the rock mass deformability and rock joint patterns. Of the parameters which have been investigated, the most important parameter was found to be the reservoir water level. The rock mass deformability which is neglected by other investigators is also found to be important. From the 3-D analyses, the failure friction angle was found to be sensitive to the assumptions made on the eastern boundary, and could affect the failure friction angle by approximately 3°. The slope was found to exhibit signs of failure beginning from $\phi_{slide\_surface}$ = 26° before complete loss of resistance at $\phi_{slide\_surface}$ = 18°. It also emerges that, although the eastern end of the slope is the first to exhibit signs of movement, the displacements at the western end of the slope become larger than the ones at the eastern end as the stability of the slope reduces.

Finally, this study showcases some useful numerical techniques developed ad-hoc for DEM analyses to investigate the stability of large-scale slopes.

Keywords: Vajont, rock slide, rock slope, strength reduction, distinct element method, kinematics

1. Introduction

The Vajont Dam, sited close to the outlet of the Vajont River in Italy (see Fig. 1), was completed in 1959. -The dam spans a very deep narrow gorge in the Vajont Valley and has a height of 266.5 m and chord length of 160 m. It was designed for a water storage level of 722.5 m a.s.l. and the base of the river was approximately 465 m a.s.l. The reservoir water level was raised since 1960, reaching its maximum in 1963. Before the catastrophic failure in 1963, there were signs of movement of the Vajont slope and an earlier slide of 700,000 m^3 had occurred on 4 November 1960. On 9 October 1963, when the resevoir level was about 700 m above sea level, an estimated rock mass volume of 200 -300 million m^3 slid off from the toe of Mount Toc into the reservoir at an estimated speed of 20-30 m/s (Müller, 1964; Ghirotti, 2006). The slide happened close to the dam and extended to as far as 1800 m upstream (East-West direction in Fig. 1). The slide surface reached an elevation of 1400 m a.sl. and as far as 1600 m away from the shores of the lake (Jaeger, 1972). Water from the reservoir overtopped the dam and flooded the Piave Valley, destroying the small town of Longarone and claiming about 2000 lives.

Since the tragedy occurred, in the last 50 years there have been numerous publications to investigate the geology of the rock slide (e.g. Müller, 1964; Müller, 1968; Müller; 1987; Broili, 1967; Belloni & Stefani, 1987; Hendron & Patton, 1985; Semenza & Ghirotti, 2000). More recent geological studies have been reported in Paronuzzi & Bolla (2012) and Wolter et al. (2014). Several analyses have been carried out employing various numerical and analytical methods (Alonso & Pinyol, 2010; Pinyol & Alonso 2010; Crosta et al., 2007; Veveakis et al., 2007; Roubtsova & Kahawita, 2006; Sitar et al., 2005; Sornette et al., 2004; Helmstetter et al., 2004; Vardoulakis, 2002). In this paper we illustrate new findings obtained via a combination of 2D and 3D DEM analyses (Cundall & Strack, 1979; Cundall, 1988) shedding light on the influence of various geometrical and mechanical parameters in the onset of the landslide and whether 3 dimensional effects are important.

In this article, ad-hoc techniques for investigating the stability of a large-scale slope using the DEM have been used. First, a robust methodology to perform strength reduction is required, so that a coherent comparison can be made for the sensitivity analysis of different physical parameters. The strength reduction technique employed in the Paper avoids the difficult task of determining a suitable criterion for loss of static equilibrium of the slope, in an automated computer routine, before the next strength reduction step is applied (Dawson et al., 1999; Itasca, 2013). In this regard, the main difficulty arises when the prescribed criterion is not satisfied after a large number of iterations, but slow convergence for quasi-static equilibrium is exhibited (Itasca, 2013); this problem is compounded by the fact that a computer routine must be automated. The second challenge is due to the fact that with the current computational power, in the case of a large-scale slope, it is not possible to model every individual rock joint. Thirdly, most investigators found that the stability of a jointed rock slope is sensitive to the block size adopted in the discontinuous analysis, and accounted for the influence of block size mainly from a kinematic viewpoint (Sitar et al., 2005; Brideau & Stead, 2012; Corkum & Martin, 2004). However, for a DEM analysis with compliant contacts, the increase in number of blocks (or smaller block size) also increases the compliance of the material if the contact stiffnesses do not change. All of these challenges have been given thoughtful consideration for the purpose of studying the Vajont slope using the DEM, and to investigate the sensitivity of the analyses to the relevant governing parameters, such as rock joint friction angle, stiffness, block size, reservoir water level, rock joint orientation and failure geometry.

2. 2-D and 3-D geological models

The analyses were run employing the open source DEM code YADE (Kozicki & Donzé, 2008) with rigid blocks and compliant contacts, i.e. according to the so-called soft contact approach. The contact detection algorithms reported in Boon et al. (2012) and Boon (2013) were used in this study, and they are based on a novel mathematical framework consisting of linear programming and the concept of analytic centre. Rather than linear programming, second order conic programming could also be used (Boon et al., 2013). The algorithms require knowledge of the linear inequalities defining the block faces only, and information on the vertices and edges are unnecessary. Likewise, for block generation, a similar novel mathematical framework, which is based on a single-level data structure consisting of block faces only, was used (see Boon et al., (2014 a)). The algorithms have been recently used to model a circular tunnel in a jointed rock mass in 2-D, and the calculated rock bolt and lining forces were found to compare well with elastic solutions (Boon et al., 2014 b).

The strength parameters suggested by the literature for the slide surface and rock mass are summarised in Tables 1 – 3. Table 1 lists the strength parameters which were deduced from laboratory experiments; Table 2 lists the estimated strength parameters adopted by the investigators for their stability or velocity analyses;

Table **3** shows the strength parameters calculated by various investigators from back analyses.

The DEM models were constructed mainly based on the published work of Broili (1967), alongside the work of Müller (1968) and Hendron & Patton (1985). The plan view of the Vajont slope in Broili (1967) is shown in Fig. 1. Sections A-A and G-G of the slope (indicated in Fig. 1) are shown in Fig. 2 and Fig. 3 respectively. A distinct feature of the Vajont slope is its chair-shaped structure, insomuch as the "back" and "seat" of the chair are well-defined. The western end (Section A-A) is chosen for analysis because it is geometrically representative of the slope, which is known to be chair-shaped, and has been established by numerous investigators to be more critical than the middle section (also chair-shaped) (Nonveiller, 1967; Hendron & Patton, 1985; Alonso & Pinyol, 2010). The eastern end was not considered in our 2-D analysis because field surveys by previous investigators suggest that the bedding planes forming the slide surface were broken-off in a step-like manner by the slide (Hendron & Patton, 1985; Broili, 1967). That is to say, the sliding of this section is likely to have sheared across intact rock (Hendron & Patton, 1985). This makes the strength reduction method on the entire slide surface less suitable for this section.

2.1 Slide surface

The slope slid on top of the strong Oolitic Vajont limestone formation (see Fig. 2 and Fig. 3). The orientation of the Oolitic limestone can help reconstruct the strata of the overlying formation (cf. Broili, 1967). According to Broili (1967, p. 63), the Oolitic limestone at the "back" of the western edge has an average dip direction of 6 - 13° and dip of 38°. At the middle-eastern area, the "back" has a dip direction of 353° and dip of 43°. Overall, the "back" of the chair-shaped slide surface has an apparent dip of 36 - 40° in the N-S direction (Broili, 1967, p. 69).

The East-West section of the "seat" of the sliding surface forms a bowl-shaped structure (see Fig. 3). The Oolitic limestone dips from 8 - 17° eastward with dip direction being 70 - 90° (Broili, 1967, p. 63). More precisely, according to Hendron & Patton (1985, p. 25), the bedding planes are steeper (17 - 22°) on the west end and flatter (10 - 11°) in the centre. The failure geometry steepens again to 30 - 40° closer to the east. The east boundary was found to be stair-stepped by Broili (1967) and Hendron & Patton (1985).

In this study, the following sliding surfaces were adopted (the notation of dip-direction/dip is used):

Back-West: 9.5°/38° (Broili, 1967)

Back-East: 353°/43° (Broili, 1967)

Seat-Centre: 80°/10.0° (Broili (1967) and Hendron & Patton (1985))

Seat-West: 80°/19.5° (Hendron & Patton, 1985)

The blocks defining the base of the slope for both the 2-D and 3-D DEM models were assigned as rigid, i.e. all degrees of freedom were constrained. In our analyses, strength reduction is performed on the faces of the blocks defining the slide surface (Fig. 4 (a)). No reduction was applied on the sliding planes extending beyond the east of the eastern fault, since they are not part of the slide surface. Note that the stair-shaped structure on the eastern end or the bowl-shaped failure surface in the East-West section (see Fig. 3) was not predefined in the DEM model here. That is to say, the "seat" of the chair (80°/10.0° in Fig. 4 (a)) was allowed to continue to dip eastward, rather than making it curve upward close to the eastern end. The breaking-off of the slope at the eastern end was allowed to develop on its own course. This assumption was made in the model, after weighing against the alternative choice of imposing the authors' conjecture of the jaggedness and orientation of the breakage at this eastern section. Further, it was considered worthwhile to allow for the possibility of the DEM model to explain whether the difference in geometrical orientation at the "back" of the western and eastern sections could indeed lead to severe geometrical distortions for the sliding mass at the eastern section, as was observed in the field.

2.2 Discontinuities and bedding planes

According to Müller (1968, p.14), two major sets of discontinuities were present. The first dips subvertically and strikes N-S. The second strikes normal to the first, i.e., about E-W, and also dips vertically. Müller (1968, p. 9) found that the layers dip generally 35 - 45° to the North. Broili (1967, p. 52) suggested that the bedding dips 45 - 50° northward and changed at the gorge to 12-18° eastward. Based on this information and the direction of the slide surface, the directions of the bedding planes in the 3-D models adopted were (the notation of dip-direction/dip is used):

Bedding planes of the "back": 0°/45°

Bedding planes of the "seat": 80°/10°

The former was chosen because it conforms to both suggestions by Müller (1968) and Broili (1967); the latter was chosen so that the bedding planes are parallel to the seat of the slide surface. The 3-D model constructed for DEM analysis is shown in Fig. 4. The orientations of the slide surface are indicated on Fig. 4 (a).

The 2-D DEM model derived from Section A-A is shown in Fig. 5. The bedding planes in the 2-D model were assumed to be parallel to the slide surface.

3. Physical properties

A schematic of the slope is shown in Fig. 6. Different strength and stiffness properties were assigned to the slide surface and rock mass, with strength reduction being performed on the slide surface only.

3.1 Slide surface

A shear softening model was used to model the shear behaviour of the clay from the fully-softened friction angle to the residual friction angle, based on published experimental data by Tika & Hutchinson (1999) (see dashed lines in Fig. 7 (a)). Also Kilburn & Petley (2003) suggest that brittle failure causing shear softening was one of the mechanisms which had taken place during the Vajont slope failure. Based on the modified data presented by Vardoulakis (2002) for his calculations, the effect of shear softening was modelled using the following expression:

$$\mu = \mu_0 - 0.0593 \times (1 - e^{-u_s / 0.35}) \tag{1}$$

where μ_0 is the nominal friction coefficient (specified through the strength reduction procedure discussed later in Section 4) and u_s is the cumulative shear displacement (units: m) along the slide surface. Fig. 7 (b) shows the shear softening model plotted against the experimental values.

The normal stiffness at the slide surface was kept at 2 GPa/m in this study. This value for the normal stiffness was selected so that it was always higher than all the shear stiffness values adopted for parametric analyses, because this is more physically realistic. The shear stiffness used in the DEM analyses was 0.1 GPa/m, unless otherwise mentioned. The shear stiffness values deduced from the results of ring shear tests (stress-displacement curves) presented in Tika & Hutchinson (1999) and Ferri et al. (2011) are in the same order of magnitude (~10^8 Pa). The thickness of their samples was between 18-20 mm, while the thickness of clay layers observed in the field varied between 1 – 20 cm (Ferri et al., 2011).

3.2 Rock mass

Since the friction angles required for stability at the slide surface calculated from back analyses in the literature (see **Table 3**) are higher than experimental measurements, the highest credible rock mass strength proposed in the literature were adopted in our reference analysis, i.e. rock mass friction angle φ = 40.0°, cohesion c = 0.787 MPa, tensile strength σ_t = 0.076 MPa, and residual values of φ = 40.0°, c = 0.0 MPa, σ_t = 0.0 MPa (see Fig. 8 (a)). The cohesive strength was chosen as in Alonso & Pinyol (2010), whereas the tensile strength was estimated using the software RocLab (Rocscience Inc., 2007) based on Hoek-Brown parameters proposed by Alonso & Pinyol (2010), i.e. uniaxial compressive strength of intact material, σ_c = 50 MPa; Geological Strength Index, GSI = 50; material constant, m_i = 9 (marls, soft limestones); disturbance factor, D = 0.5 (Hoek et al., 2002)) at a normal stress of 2 MPa.

The Vajont rock slope is heavily jointed with respect to the scale of the slope, so that with the current computational power it is unfeasible to model the actual joint spacing. When viewed as an equivalent intact rock mass, the elastic modulus of the rock mass can be estimated from the software RocLab (Rocscience Inc, 2007) using the Hoek-Brown parameters suggested by Alonso & Pinyol (2010) (see Section 3.2.1 for the parameters). The disturbance parameter D, used as a degradation parameter in Alonso & Pinyol (2010) to derive the strength at the shear plane between the 'back' and the 'seat' of the chair, was ignored here in order to derive more realistic rock mass deformability values reflecting the global stiffness of the slope. The shear modulus can, in turn, be estimated from the deformation modulus and a typical value of Poisson's ratio for limestone. The Young's modulus and shear modulus of the jointed rock mass were taken to be 7680 MPa and 3072 MPa respectively; the latter was calculated using a Poisson's ratio of 0.25.

Because the distinct element method does not model the rock mass as a continuum (rigid blocks were employed in this model), the rock mass deformation modulus cannot be used directly. The deformation of the rock mass in this numerical model is captured through joint deformations.

The joint stiffness in the DEM was scaled according to the mean joint spacing, s_{mean}, to match the rock mass deformation properties using the following equations (Goodman, 1989):

$$k_{\mathrm{n}} = \frac{E}{s_{\mathrm{mean}}} \tag{2}$$

$$k_{\mathrm{s}} = \frac{G}{s_{\mathrm{mean}}} \tag{3}$$

with k_{n} and k_{s} being the normal and shear joint stiffness per unit area. Table 4 shows the stiffness values adopted with the mean joint spacings. This technique of scaling the contact stiffness with joint spacing is conceptually illustrated in Fig. 9.

The water level was assumed to be horizontal, with only the effect of buoyancy being modelled. Buoyancy was introduced by applying a vertical upward force, F^{u}, which is proportional to the submerged volume of the blocks based on Archimedes' principle.

$$F^{\mathrm{u}} = \rho_{\mathrm{w}} V_{\mathrm{submerged}} g \tag{4}$$

where ρ_{w} is the density of water, g is the gravity acceleration and $V_{\mathrm{submerged}}$ is the submerged volume of the solid.

4. Strength reduction analyses

Traditional strength reduction in finite difference (or finite element) simulations explicit over time (e.g. FLAC) is based on imposing strength reduction steps, each step being imposed after a static equilibrated configuration has been found on the basis of certain tolerance criteria, e.g. unbalanced forces, displacement increments, kinetic energy or number of iterations (e.g. Itasca, 2013; Dawson et al., 1999). In order to define failure, either one of these criteria is used or a threshold on the cumulative displacement determined based on operational requirements in the field is employed (Diederichs et al., 2007). However, it is difficult to provide a physical justification regarding the values adopted for the tolerance criteria. Furthermore, often the obtained strength parameters are dependent on the tolerance values adopted. Finally, often cases of slow convergence where the tolerance criteria are not satisfied after many time-steps are encountered (Itasca, 2013). These cases normally require a set of ad-hoc problem-specific tolerance criteria and large simulation runtimes.

In our analyses, the aforementioned problems with specifying and satisfying the tolerance criteria are overcome with a different way of performing strength reduction. The friction angle was reduced by a very small amount at each time step, *i.e.* at a constant rate. Displacements increase gradually with strength reduction (executed at every time step). The critical friction angle was determined from the displacement vs friction angle curves, with failure assumed to occur when a sharp increase of displacement takes place. For this method to provide meaningful results, it is necessary to establish that the rate of strength reduction is low enough for force redistribution to take place and that the simulation is not dominated by dynamic effects (e.g. see Utili and Nova, 2008; Utili and Crosta, 2011).

5. Results and discussion

5.1 Two-dimensional analyses

The parameters used in the reference analysis are summarised in Table 5. In the DEM calculations, a linear elastic-perfectly plastic contact law was used to model the shear behaviour of the contacts, and a linear elastic contact law was used to model the stress-displacement behaviour in the normal direction. The shear softening contact law described in Eq. (1) was used to model the slide surface in this reference analysis. The numerical implementation–of the contact law in the DEM code is described more comprehensively in Boon (2013). A suitable time step of 0.001 sec/step was established (Boon, 2013). The slope model was generated with local damping until the kinetic energy, unbalanced forces and slope displacements were sufficiently low, before the strength reduction process was carried out. At this stage, local damping was removed and linear viscous damping at the contacts was activated.

From a simulation runtime point of view, it is desirable to use the highest strength reduction rate possible. Fig. 10 shows the influence of the rate of strength reduction on the slope response. The response in terms of displacement-friction angle is more abrupt at failure for low strength reduction rates (Fig. 10). The results showed that a strength reduction rate of 0.025 °/sec is reasonable, because the results were very close to the critical friction angle given by a lower strength reduction rate, 0.0125 °/sec ($\phi_{slice\_surface}$ = 20.6 - 20.8°).

The choice of damping ratio (Table 5), i.e. ξ = 0.1, has been underpinned by a parametric analysis carried out for various damping ratios. From the results it emerges that the friction angle required for stability decreases with the value of viscous damping ratio. Fig. 11 shows that the undamped model experienced substantial displacements from the beginning of strength reduction. A detailed discussion on the reasons of this behaviour is provided in Boon (2013). The simulation with a minimal damping ratio of 0.01 also failed much earlier than the other simulations which were run with larger damping ratios. Note that some researchers have also found that it was necessary to use at least a very small damping ratio to model an undamped system, i.e. to prevent rounding errors from affecting the simulations (Kveldsvik et al., 2009; O'Donnovan et al., 2012). For larger viscous damping ratios (ξ =0.05 - 0.5, believed to be a range of practical engineering interest (Buzzi et al., 2012; Durda et al., 2011)), the difference in the critical friction angles from the case of ξ = 0.1 was little, i.e. approximately ±0.15°, which is smaller than the effects of uncertainties concerning other parameters of the model.

5.1.1 Comparison with Sitar et al. (2005)

In this section our DEM simulations are compared with the DDA analysis run by Sitar et al. (2005). The friction angle of the vertical discontinuities was assigned as 40° with zero cohesion and tensile strength. These values were not explicitly mentioned in Sitar et al. (2005) for their stability analysis, but were adopted from Hendron & Patton (1985) since the results of Hendron & Patton (1985) with interslice friction angles of 40° (rather than 30°) was explicitly used as a benchmark study in Sitar et al. (2005). The contact law was elastic-perfectly plastic, the reservoir level was below the slide surface (dry condition), and the number of blocks in the model was 233. The contact stiffness (both rock joints and slide surface) in the normal and shear directions were 0.75 GPa/m and 0.37 GPa/m respectively. These were derived from an elastic modulus of 30 GPa and a Poisson's ratio of 0.02 used in their numerical model, for the joint spacing used for this comparison exercise (40 m). The reason for using a low Poisson's ratio was not mentioned by the investigators. Note that the DDA method does not model the deformability of the rock joints because the method imposes a non-penetration rule between contacts. In Sitar et al. (2005), the critical friction angle is 15° for 23 blocks and 16° for 105 blocks. In our model, the critical sliding friction angle was found to be 16.6°, at which the slope experienced an abrupt and large displacement (see Fig. 12). The difference is marginal and can be attributed to the different assumptions made in the numerical methods: rigid blocks with compliant contacts have been used in our DEM simulations whereas deformable blocks with non-compliant contacts were used in the DDA models by Sitar et al. (2005).

5.1.~~5~~2 Influence of the number of blocks

The number of blocks generated from mean spacings of 20 m, 30 m, 40 m, 60 m, 80 m and 120 m are shown in Table 6. Fig. 13 (a) shows the influence of joint spacing whilst Fig. 13 (b) shows the results in terms of block number (log-scale). Note that the stiffness employed for the rock joints has been prescribed according to Eqs. (2) and (3) in order to keep the same rock mass deformability in the analyses performed. Thus the difference in the obtained results can be mainly attributed to the geometrical effects arising from the size of the blocks.

In case of less than 100 blocks (Fig. 13 (b)), the slope becomes more prone to failure as the number of blocks increases, i.e. the friction angle required for stability increases. This trend is consistent with the results obtained by Sitar et al. (2005). For more than 100 blocks, the friction angle required for stability is no longer sensitive to the number of blocks. Note that the approximated critical friction angle estimated by Paronuzzi et al. (2013) for one of the western sections of the slope is 20.5°, ~~and~~ which is very close to the results ~~here~~ obtained here.

5.1.~~6~~3 Influence of water level

The influence of the water table was investigated by studying the value of friction angle required for stability (Fig. 14). This increases with the height of the water table, and is consistent with the findings of other investigators. The friction angle required for stability with 90 m water level (*el.* 710 m a.s.l.) above the slide surface (20.6°) ~~is~~ was found to be 1.8° higher than under dry conditions (18.8°). The influence of water level was also found to be minimal by other investigators, i.e. raising the water level to 700 m a.s.l. required an increase of friction angle ranging between 1.0 - 2.7° for stability (Kenney, 1967; MacLaughlin, 1999; Alonso & Pinyol, 2010; Paronuzzi et al., 2013). The difference in critical friction angles between dry and wet conditions calculated by Sitar et al. (2005) was larger, i.e. 4 – 5°, because the pore pressure was assumed to be 0.3 times the overburden pressure. It can be seen from Fig. 14 that the rise in failure friction angle, $\Delta\varphi$, is greatest when the water level increases from 0 – 30 m ($\Delta\varphi$ = 1.0°) than 30 –60 m ($\Delta\varphi$ = 0.4°) or 60 – 90 m ($\Delta\varphi$ = 0.4°). This observation is consistent with the analytical calculations presented by Alonso & Pinyol (2010), in which the factor of safety for the slope was shown to decrease with the rise of the water level in a non-linear manner. A possible explanation is that, as the water level increases, a larger fraction of the material driving the slope to failure is also submerged at the same time.

5.1.4 Influence of slide surface stiffness

Fig. 15 shows the influence of the slide surface shear stiffness, k_s, on the friction angle required for stability. Simulations were run for shear stiffness values ~~of~~ ranging from 0.01 GPa/m to 1.8 GPa/m. Instead, the stiffness assigned to the rock joints away from the failure surface was constant and it is reported in Table 5. The friction angles required for stability fluctuate between 20.2 - 20.6°, and they are almost independent of the shear stiffness of the slide surface. This is not surprising since, for failures which involve displacement of material along a slip surface, the stiffness of the slip surface is not normally considered in routine design calculations in geotechnical practice. Because strains are concentrated along the slip surface, the available resistance at the slip surface is not constrained by its stiffness, i.e. the slope just needs to displace a different amount depending on its stiffness.

5.1.~~8~~ 5 Influence of rock mass deformability

In this set of simulations, the influence of rock mass deformability ~~is~~ was investigated by varying the stiffness values of the contacts between rock blocks while keeping the stiffness along the failure surface constant. Fig. 16 shows that the critical sliding friction angle at the slide surface is sensitive to the rock mass deformability. The equivalent rock mass deformability (horizontal axis in Fig. 16) was derived from Eqs. (2) and (3). The stiffer the rock mass, the larger the slope resistance against sliding. Looking at Fig. 17, the critical friction angle is approximately proportional to Log_{10} of the equivalent stiffness. This relationship is in contrast with that for the slide surface shear stiffness, in which ~~its~~ has only a minor influence on the slope stability (the slope stability is almost independent of the shear stiffness of the slide surface). It is noteworthy that both observations are consistent with the analysis of the Carsington embankment failure using finite element analysis of Potts et al. (1990), who found that:

> *"First, increasing the pre-peak foundation stiffness by a factor of 2 decreases failure elevation and safety factor by small amounts, as a more rigid base to the yellow clay layer concentrates strain in it."*
>
> *"Seventhly, the stiffness of the mudstone fill has a significant effect, an increase by 2.5 times reducing progressive failure and increasing the safety factor by about 4%."*

Comparing with the case of Carsington Embankment, the increase in stiffness of the rock mass by 2.5 times for the Vajont rock slope was found to decrease the failure friction angle by approximately 2.7% (0.56 °), the same order of magnitude as observed by Potts et al. (1990). It is possible that the greater kinematic constraint afforded by a stiffer rock mass could increase the slope resistance to sliding. While the stability of the slope is almost independent of the slide surface shear stiffness (due to the scatter of the data points), the gradient of the best-fit line (plot of failure friction angle against shear stiffness) in Fig. 17 is positive. This suggests that the Vajont slope becomes less stable as the slide surface becomes stiffer, i.e. more brittle.

5.1.~~9~~ 6 Influence of rock joint friction angle

The sensitivity of the stability of the slope to the rock joint friction angle values was investigated. The results (see Fig. 18) show that ~~the~~ decreasing the rock joint friction angle from 40° to 30° increases the failure slide surface friction angle by approximately 0.6° (3 %). This result is consistent with the DDA results of MacLaughlin (1997), in which the slide surface friction angles at failure were more critical by 1° for the rock joint friction angle decreasing from 40° to 30° in the dry case, and no detectable difference (with precision of ±1° in her analysis) in the case in which the reservoir is filled (Table 6.2 in MacLaughlin, 1997). In Hendron & Patton (1985), decreasing the rock joint friction angles from 40° to 30° reduced the slope factor of safety by 10%. The factor of safety used in Hendron & Patton (1985) is the ratio of the strength of the slide surface to the strength required for translational force equilibrium (only). It is well-known in slope stability analysis that force equilibrium calculated using the method of slices is sensitive to the assumptions made on the inter-slice forces. On the other hand, moment equilibrium is less sensitive to the assumptions on inter-slice forces. Overall equilibrium is satisfied when both force and moment equilibriums are satisfied. It is therefore reassuring that, compared to the analytical calculations carried out by Hendron & Patton (1985), the results of the discontinuum numerical calculations which satisfy both force and moment equilibriums are less sensitive to the inter-slice friction angles.

5.1.~~10~~ 7 Influence of rock joint orientation

In the previous simulations, as with Sitar et al. (2005) and MacLaughlin (1997), the joints across the bedded structure were vertical. In Broili (1968), although it was maintained that the major faults and joints were vertical, there was a mention that shear faults dipping 40° - 50° South were observed at the bend between the back and the seat of the “chair”. In Alonso & Pinyol (2010), a shear plane (used in their stability analysis) was assumed to form at the bisector plane (dip angle ≈ 70°) between the seat and the back of the chair to maintain kinematic compatibility between the upper and lower wedges of the slope. Here, the influence of the joint orientations along which shearing takes place was investigated (dip angle = 50° and 70°).

It is also of interest to investigate the influence of the dip angle of sub-horizontal beddings on the results. Because 2-D cross-sections for a slope are normally assumed to be parallel to the sliding direction, the apparent dip angles may vary depending on the angle that was subtended between the sliding direction and the dip-direction of the bedding plane (see Fig. 19 for illustration). This concept was also used in Gens & Alonso (2006) to study the Aznalcóllar dam failure. It is worth to recall that for the Vajont slope, the “seat” of the chair is dipping East approximately but the slope slides towards North. In the numerical study here, a dip angle of 1.8° was adopted; it corresponds to an apparent dip angle which may arise from a true dip angle of 10° with the sliding direction being near-perpendicular to the dip direction (±10° from perpendicular, i.e. α = 80° in Fig. 19). In our model, the seat of the “chair” was assumed to be inclined parallel to the bedding planes.

The results, plotted in Fig. 20, suggest that an inclined cross-joint with dip angles of 50° and 70° are less critical than a vertical discontinuity by approximately 1.7° and 1.1° respectively. This finding is consistent with the conventional geotechnical engineering practice of using vertical slices when performing limit equilibrium calculations for the stability of slopes and embankments. Compared to the previous analysis with horizontal bedding planes, an increase in the sub-horizontal bedding plane inclination by 1.8° gives rise to an increase in friction angle required for stability of approximately 0.5°. This study suggests that the critical friction angle for a jointed rock slope with a non-planar slip-surface is sensitive to its joint patterns.

5.1. 8 Failure mechanisms obtained

The resistance afforded by the rock mass when the slope approaches failure can be ~~seen~~ inferred from the contact forces shown in Fig. 21. Many investigators speculated that the sudden collapse observed in the field is related to the resistance afforded by the rock mass (Mencl, 1966a; Mencl, 1966b; Hutchinson, 1987; Alonso & Pinyol, 2010). As the rock mass slid pass the "bend" between the back and the seat of the slope, arching was observed across the bend with a corresponding loss of lateral contacts between the blocks underneath the arch (see Fig. 21 (c)). This behaviour is in agreement with the speculation by Mencl (1966b) on the formation of a cavity at the bend with a corresponding zone of arching. As displacement accumulated, separations between rock strata appeared, and a large tensile opening was created across the rock strata (see Fig. 22 (a)). This was also observed in DDA simulations of Sitar et al. (2005). The failure modes of the inclined joints investigated in the previous section are shown in Fig. 22 (b) and (c). For a chair-shape slope, it appears that tensile failure is a possible failure mechanism when the shear resistance across discontinuities is high. This is not surprising for jointed rock masses because their tensile strength is almost non-existent.

However, for rock joint friction angles 30° and below, shearing across the rock joints turned out to be the predominant failure mechanism, even for large displacements (see Fig. 22 (d)). As noted in Kiersch (1964), field observations indicate that tensile openings were present at the slope surface but they were not as pronounced as in Fig. 22 (a). Rather, the slope was found to move more uniformly as in Fig. 22 (d) (rock joint friction angle 30°). This suggests that the residual rock mass friction angle at failure (after large ~~straining~~ displacements) in the field is likely to be closer to 30°. Note that strength degradation of the rock mass was indirectly implied by Hendron & Patton (1985) and Anderson (1985) who adopted lower friction angle values in their kinematic analyses. Strength degradation in terms of rock mass shear strength was also suggested by Alonso & Pinyol (2010).

5.2 Three-dimensional analyses

In this 3-D model (see Fig. 4), the joint spacing is set to 80 m, and the joint normal and shear stiffness are 0.096 GPa/m and 0.0384 GPa/m respectively. The slide surface normal and shear stiffness are 2 GPa/m and 0.1 GPa/m respectively. Two vertical eastern faults were introduced into the model, with dip directions 0° and 110° respectively (see Fig. 4(a)). The rock joint friction angles are 40° while the friction angles of the eastern faults were set to 36° (Hendron & Patton, 1985, p. 61), both of which adopt the elastic-perfectly plastic contact model in the shear direction. The higher credible rock joint friction angle (40°) was employed in our 3-D analyses with the aim of resolving the discrepancy between the measured slide surface friction angle and the back-calculated values reported in the literature (see Tables 1 and 3).

Two types of analyses were run. The first employed strength reduction on the slide surface to bracket the failure friction angle, as in the 2-D case. The rate of strength reduction employed is the same as that used in 2-D, i.e. 0.025°/s, unless otherwise mentioned. The second analysis involves generating the slope at a specified friction angle, with a reservoir water level before filling, i.e. 460 m a.s.l. Thereafter, the water level was raised gradually. The water table was assumed to be horizontal. The time-step used in 2-D (0.001 sec/step) was found to be still suitable for the 3-D model (Boon, 2013).

5.2.2 Influence of eastern boundary and reservoir water level

From Fig. 23, it is worth highlighting that, compared to the 2-D case, the slide behaviour is more ductile. This result is reasonable because, in 3-D, there exists larger kinematic freedom of movement for the rock mass. Conversely, in 2-D, movement is constrained to a plane, and failure is more abrupt. Because of the ductile failure mechanism in Fig. 23, it is difficult to define the failure friction angle precisely. In fact apart from rigid-perfectly plastic materials, ascertain failure loads for engineering structures which exhibit non-linear load-displacement behaviours is not straightforward.

The differences between collapse and safe loads for a footing foundation have been discussed in Atkinson (2007). It will be helpful therefore to analyse the results here for the Vajont slope using the same concepts.

With rigid (kinematically constrained) eastern boundaries and reservoir water level 710 m a.s.l. (solid line in Fig. 23), onset of failure was observed at approximately 26°. The ultimate failure friction angle, associated with complete loss of resistance, is approximately 18°. From Fig. 23, friction angles above 20° appear to be safe. Note that in Crosta et al. (2007), the friction angle required for stability for the same reservoir water level and rock joint friction angle was found to be approximately 19°.

Fig. 23 shows ~~that~~ the results of strength reduction for the slope with rigid and non-rigid eastern boundaries, i.e. with and without restricted kinematic freedom (see Fig. 4 (a)). For the non-rigid eastern boundaries, the blocks to the east of the eastern faults are allowed to slide on the basal blocks defining the slide surface (Section 2.1). However, let us recall that strength reduction was not performed for the basal blocks on the east of the eastern faults. The result confirms that the additional shear resistance of the eastern boundary hypothesised by Hendron & Patton (1985) is important. The displacement-strength curve for a non-rigid eastern boundary is approximately 3° more critical than the case with rigid eastern boundaries. Instead of viewing the this comparison in terms of the "contribution" from the eastern boundary, an alternative way of interpretation is in terms of the slide surface geometry, i.e. the blocks which are kinematically constrained to define the failure boundaries.

For a lower reservoir water level of 460 m a.s.l., i.e. before the filling of the reservoir, the curve is approximately 1.5° less critical than the case with reservoir water level 710 m a.s.l. The observed influence of the water level compares well with the 2-D case (approximately 1.8°).

Although the geologically complex Vajont rock slope is simplified in our 3-D model (Fig. 4), the model captures the essential geometrical features of the slope. There is interesting insight that the slope at different sections did not move uniformly (see Fig. 24). At high slide surface friction angles, the eastern end of the slope experienced larger movements compared to the centre and western ends of the slope (see Fig. 24 (b)). For friction angles smaller than approximately 23° (closer to ultimate failure), the cumulative displacements at the western end of the slope were larger than the eastern end. It is interesting to note that from field measurements (Müller, 1964), the western end of the slope experienced larger displacements than the eastern end. However, from the 2-D back analyses by Hendron & Patton (1985) and Paronuzzi et al. (2013), the eastern end of the slope was found to be more critical than the western end. This discrepancy is largely due to the assumption of the slope and slide surface geometry in their calculations. The 3-D results in Fig. 24 can explain these contradictory results in terms of kinematics. Although signs of instability were observed first at the eastern end in our model, the loss of stability in the eastern end does not lead to an abrupt failure. In fact, the eastern end of the slope is capable of redistributing the forces to arrest failure. The western end of the slope is more prone to sliding, and experiences greater displacements than the eastern end with subsequent strength reduction.

The failure friction angle (between 18 - 26°) in this 3-D study is nowhere near 12° as suggested by Hendron & Patton (1985). It is still a topic of debate as to whether the actual shear strength of the clayey slide surface reached residual values (Vardoulakis, 2002) after the first slide, and whether there was strength recovery.

5.2.3 Influence of rising reservoir water level

According to field measurements, the slope experienced creep with some accelerated phases up to approximately 3 m before the actual slide (Müller, 1964). The actual slide collapse was believed to be triggered by the velocity softening effect at the clay layer (cf. Ferri et al. (2011)); the slope experienced some movement with reservoir water filling, and the slope movement hit a critical velocity beyond which it could not be arrested even though the reservoir water level was lowered. Because the ultimate collapse of the slope depends on the shearing velocity at the slide surface, it is not easy to establish the exact value of slide surface friction angle for which this phenomenon could have taken place. In fact, as long as there are any signs of movement indicating instability, the slope has a great risk of sliding.

3-D simulations were carried out to model more realistically the situation before the actual Vajont slide took place. The simulations were carried out using two peak slide surface friction angle values, i.e. 26° and 21°. These friction angles were above the ultimate failure friction angles for the case of reservoir water level 460 m and 710 m a.s.l. (see Fig. 25). The initial water level was assigned as 460 m a.s.l. for each simulation, and the water level was increased over time (red line in Fig. 25). The rate of reservoir filling was 0.25 m/s. The raising of the water level is not modelled at the same rate as the actual filling of the reservoir, because soil or hydraulic models capable of capturing rate effects are not used here (see Panoruzzi et al., 2013). Note that this water level raising rate has a gentler influence on the slope than the strength reduction rate of 0.025°/s that was adopted in the previous analysis. This can be inferred from Section 5.1.3 in which the slope became more critical by 1.8° when the reservoir water level was raised by 90 m. Like all the previous simulations, the slope was generated with local damping until the kinetic energy, unbalanced forces and slope displacements were sufficiently low, after which local damping was removed and viscous damping at the contacts was activated. The raising of the water level was then carried out. Shear softening of the stiff clay layer (Eq. (1)) was allowed to take place, but the effect of shear softening with velocity was not studied here (cf. Ferri et al., 2011). The results for the peak slide surface friction angles 26° and 21° are shown in Fig. 25 (a) and (b) respectively. The results show that for peak slide surface friction angle of 26°, the eastern end of the slope initially experienced larger displacements compared to the western end. For peak slide surface friction angle of 21°, the western end of the slope experienced larger displacements, which is more consistent with field measurements. In fact, Belloni & Stefani (1987) has conjectured that the failure mechanism of the slope is complex at its limiting condition, because the potential mechanism for further loss of resistance could be affected by the slope's lateral constraints and overall geometry. A change in failure mode at the limiting condition was also considered possible in Belloni & Stefani (1987). A similar observation can be inferred from Fig. 25 (a). The displacement of the western end was initially smaller than the eastern end, but eventually becomes greater than the eastern end as the reservoir water level is raised further.

5.2.4 Discussion of failure shape

Recall that the discordance between bedding planes at the eastern "seat" of the slope and the bowl-shape of the slide surface perpendicular to the slide direction was highlighted by Broili (1967) and Hendron & Patton (1985). In the DEM simulations, angular distortion was also observed at the eastern periphery/boundary of the slope (H-H section of failed slope in Fig. 26 (a) is shown in Fig. 26 (c)). In Fig. 26 (a), separations and relative rotations between rock blocks can be observed towards the eastern end; and the rock blocks towards the centre and western areas are arranged more uniformly. In Fig. 26 (b), the displacements experienced by each block are plotted. The results are in agreement with the field measurements presented in Müller (1964) and the observation that the western end of the slope was moving "en masse" (Belloni & Stefani, 1987). As shown in Fig. 26 (c), because of the geometrical discordance between the different sections of the slide surfaces, the rock slope did not shear entirely along the weaker eastern fault ($\phi_{eastern\_fault} =$ 36° compared to ϕ_{joint} = 40°).

6. Conclusions

The Vajont rock slide was studied using the distinct element method (DEM) in 2-D and 3-D. This study was carried out mainly using strength reduction. This strength reduction technique is based on performing strength reduction at every time step. A suitable and small-enough strength reduction rate can be established by repeating the simulations with a few strength reduction rates. This is conceptually more robust and straightforward than conventional techniques for which it is necessary to specify several tolerance criteria which could be difficult to justify and numerically slow to converge. Further, the technique to preserve the overall slope deformability as the number of blocks is increased was also presented.

Overall, the friction angles required for stability obtained from the DEM calculations were higher than the 12° suggested by Hendron & Patton (1987) from site investigations (they suggested that an additional 2° should be added to the measured 10° to account for the influence of rock asperities since the clay thickness varies at the slide surface). The 2-D DEM models led to similar conclusions as 2-D limit equilibrium analyses presented by other researchers. The results of the 2-D numerical study show that the most important parameter affecting the slope stability is the reservoir water level. The study also shows that because of the peculiar shape of the slope and slide surface, the rock mass deformability which has been hitherto neglected by other investigators is important.

The 3-D results show that the shear resistance afforded by the eastern boundary is significant; the friction angle required for stability was found to be approximately 3° lower compared to the case when the eastern boundary was non-rigid. However, the back calculated failure friction angles (for the reservoir water level 710 m a.s.l.) for both 3-D and 2-D are above 12°, i.e. the value suggested by Hendron & Patton (1987) for the slip surface with clay layers. In 2-D, the failure friction angle was found to be approximately 20.6° for the western section (A-A in Broili, 1967). The determining of failure is more difficult in 3-D, because the slope behaviour was found to be ductile and non-uniform across the slope. The strength of the slope was found to be completely lost at 18°, but was found to exhibit signs of failure, i.e. large displacements, from 26° onwards. This is more representative of the field condition in which the slope was moving (or failing) progressively with the raising of water level, rather than sliding abruptly. The actual collapse is believed to be triggered by the shear softening effect with velocity (Ferri et al., 2011), which could take place between the friction angles bracketed from the 3-D simulations in this study, i.e. between 18 - 26°. As the slope stability becomes more critical, the western end of the slope was found to experience resistance loss in a more progressive manner than the eastern end.

Finally, we must note that we used a simplified geometry that cannot represent exactly the real case. The critical friction angle values and magnitude of displacement obtained in this analysis could be affected by slight changes in the failure surface geometry. Nevertheless, this study evidences the sensitivity of such type of slopes and models to some specific geometrical constraints and certain combinations of mechanical parameters.

References

Alonso, E. E. & Pinyol, N. M. (2010). Criteria for rapid sliding I. A review of Vaiont case. *Engineering Geology* **114**, 198-210.

Anderson, D. L. (1985). Static slope analysis method used for the Vaiont slide analyses. In: Hendron JR, A. J. & Patton, F. D. (eds.) *The Vaiont slide, a geotechnical analysis based on new geologic observations of the failure surface*. Washington: US Army Corps of Engineers.

Belloni, L. G. & Stefani, R. (1987). The vajont slide: instrumentation- Past experience and the modern approach. *Engineering Geology* **24**, 445-474.

Boon, C. W. 2013. The Distinct Element Modelling of Jointed Rock Masses: Algorithms and Their Verification. D.Phil. Thesis. University of Oxford.

Boon, C. W., Houlsby, G. T. & Utili, S. (2012). A new algorithm for contact detection between convex polygonal and polyhedral particles in the discrete element method. *Computers and Geotechnics* **44**, 73-82.

Boon, C. W., Houlsby, G. T., & Utili, S. (2013). A new contact detection algorithm for three dimensional non-spherical particles. *Powder Technology* S.I. on DEM, **248**: 94-102.

Boon, C. W., Houlsby, G. T., & Utili, S. (2014 a). A novel rock slicing algorithm based on linear programming. *Computers and Geotechnics* (under review).

Boon, C. W., Houlsby, G. T. & Utili, S. (2014 b). Designing tunnel support in jointed rock masses via the DEM. *Rock Mechanics and Rock Engineering*. Available online.

Brideau, M.-A., Stead, D. (2012). Evaluating kinematic controls on planar translational slope failure mechanisms using three-dimensional distinct element modelling. *Geotechnical and Geological Engineering* **30**, 991-1011.

Buzzi, O., Giacomini, A., & Spadari, M. (2012). Laboratory investigation on high values of restitution coefficients. *Rock Mechanics and Rock Engineering* **45**, No 1, 35-43.

Broili, L. (1967). New knowledge on the geomorphology of the Vaiont slide slip surface. *Rock Mechanics and Engineering Geology* **5**, 38-88.

Chowdhury, R. (1978). Analysis of the Vaiont slide - new approach. *Rock Mechanics Felsmechanik Mecanique des Roches* **11**, 29-38.

Corkum, A. G., Martin, C. D. (2004). Analysis of a rock slide stabilized with a toe-berm: a case study in British Columbia, Canada. *International Journal of Rock Mechanics & Mining Sciences* **41**, 1109-1121.

Crosta, G. B., Frattini, P., Imposimato, S. & Roddeman, D. 2007. 2D and 3D numerical modelling of long run out landslides - the Vajont case study. In: CROSTA, G. B. & FRATTINI, P. (eds.) *Risk mitigation for earthquakes and landslides report* 2007/01.

Cundall, P. A. (1988). Formulation of a three-dimensional distinct element model--Part I. A scheme to detect and represent contacts in a system composed of many polyhedral blocks. *International Journal of Rock Mechanics and Mining Sciences & Geomechanics Abstracts* **25**, 107-116.

Cundall, P. A. & Strack, O. D. L. (1979). Discrete numerical model for granular assemblies *Geotechnique* **29**, 47-65.

Dawson, E. M., Roth, W. H. & Drescher, A. (1999). Slope stability analysis by strength reduction. *Geotechnique* **49**, 835-840.

Diederichs, M. S., Lato, M., Hammah, R. & Quinn, P. (2007). Shear strength reduction (SSR) approach for slope stability analyses. In: Eberhardt, E., Stead, D., & Morrison, T. (eds.) *Proceedings of the 1st Canada-US Rock Mechanics Symposium, Vancouver-Canada*, 27-31 May 2007. Taylor & Francis, 319-327.

Durda, D. D., Movshovitz, N., Richardson, D. C., Asphaug, E., Morgan, A., Rawlings, A. R., & Vest, C. (2011). Experimental determination of the coefficient of restitution for meter-scale granite spheres. *Icarus* **211**, No 1, 849-855.

Ferri, F., Di Toro, G., Hirose, T., Han, R., Noda, H., Shimamoto, T., Quaresimin, M. & De Rossi, N. (2011). Low- to high-velocity frictional properties of the clay-rich gouges from the slipping zone of the 1963 Vaiont slide, northern Italy. *Journal of Geophysical Research - Solid Earth* **116**, B09208.

Gens, A. & Alonso, E. E. (2006). Aznalcóllar dam failure. Part 2: Stability conditions and failure mechanism. *Geotechnique* **56**, 185-201.

Ghirotti, M. (2006). Edoardo Semenza: the importance of geological and geomorphological factors in the identification of the ancient Vaiont landslide. In: Evans, S. G., Scarascia, Mugnozza, G., Strom, A., & Hermanns, R. L. (eds.) *Landslides from Massive Rock Slope Failure*. Springer. Part 5, 395-406.

Helmstetter, A., Sornette, D., Grasso, J.R., Andersen, J.V., Gluzman, S. & Pisarenko, V. (2004). Slider block friction model for landslides: Application to Vaiont and La Clapiere landslides. *Journal of Geophysical Research - Solid Earth* **109**, B02409.

Hendron, Jr A. J. & Patton, F. D. 1985. Vaiont slide, a geotechnical analysis based on new geologic observations of the failure surface. Technical Report - US Army Engineer Waterways Experiment Station.

Hendron Jr A. J. & Patton, F. D. 1987. The Vaiont slide - A geotechnical analysis based on new geologic observations of the failure surface. *Engineering Geology* **24**, 475-491.

Hutchinson, J. N. (1987). Mechanisms producing large displacements in landslides on pre-existing shears. *Memoir of the Geological Society of China*, No 9, 175-200.

Itasca (2013). 3DEC 3-dimensional distinct element code, ver 5.0. Itasca Consulting Group Inc. Minneapolis, MN.

Jaeger, C. (1979). *Rock mechanics and engineering*, Cambridge university press.

Kenney, T. C. (1967). Stability of the Vajont valley slope, discussion of a paper by L. Muller (1964) on the rock slide in the Vajont valley. *Rock Mechanics and Engineering Geology* **5**, No 5, 10-16.

Kiersch, G. A. (1964). Vajont reservoir disaster. *Civil Engineering* **34**, No 3, 32-39.

Kozicki, J., & Donzé, F. V. (2008). A new open-source software developed for numerical simulations using discrete modeling methods. *Computer Methods in Applied Mechanics and Engineering* **197**, No 49-50, 4429-4443.

Kveldsvik, V., Kaynia, A. M., Nadim, F., Bhasin, R., Nilsen, B. & Einstein, H. H. (2009). Dynamic distinct-element analysis of the 800m high Åknes rock slope. *International Journal of Rock Mechanics and Mining Sciences* **46**, No 4, 686-698.

Kilburn, C. R. J. & Petley, D. N. (2003). Forecasting giant, catastrophic slope collapse: Lessons from Vajont, Northern Italy. *Geomorphology* **54**, 21-32.

Lo, K. Y., Lee, C. F. & Gelinas, P. (1972). Alternative interpretation of the Vaiont Slide. In *Stability of Rock Slopes*, ed. E. J. Cording, 595-623.

Mencl, V. (1966a). The influence of stiffness of a sliding mass on the stability of slopes. *Rock Mechanics and Engineering Geology* **4**, 127-131.

Mencl, V. (1966b). Mechanics of landslides with non-circular slip surface with special reference to the Vaiont slide. *Geotechnique* **16**, 329-337.

Müller-Salzburg, L. (1964). The rock slide in the Vajont valley. *Rock Mechanics and Engineering Geology* **2**, 148-212.

Müller-Salzburg, L. (1968). New considerations on the Vaiont slide. *Rock Mechanics and Engineering Geology* **6**, 1-91.

Müller-Salzburg, L. (1987). The vajont catastrophe- A personal review. *Engineering Geology* **24**, 423-444.

Nonveiller, E. (1967). Shear strength of bedded and jointed rock as determined from the Zalesina and Vaiont slides. *Proceedings of the Geotechnical Conference*, Oslo.

Nonveiller, E. 1987. The vajont reservoir slope failure. *Engineering Geology* **24**, 493-512.

O'Donovan, J., O'Sullivan, C. & Marketos, G. (2012). Two-dimensional discrete element modelling of bender element tests on an idealised granular material. *Granular Matter* **14**, 733-747.

Paronuzzi, P. & Bolla, A. (2012). The prehistoric Vajont rockslide: An updated geological model. *Geomorphology* **169**, 165-191.

Paronuzzi, P., Rigo, E. & Bolla, A. (2013). Influence of filling-drawdown cycles of the Vajont reservoir on Mt. Toc slope stability. *Geomorphology* **191**, 75-93.

Pinyol, N. M. & Alonso, E. E. (2010). Criteria for rapid sliding II. Thermo-hydro-mechanical and scale effects in Vaiont case. *Engineering Geology* **114,** 211-227.

Roubtsova, V. & Kahawita, R. (2006). The SPH technique applied to free surface flows. *Computers and Fluids* **35**, No 10, 1359-1371.

Semenza, E. & Ghirotti, M. (2000). History of the 1963 Vaiont slide: The importance of geological factors. *Bulletin of Engineering Geology and the Environment* **59**, 87-97.

Sitar, N., MacLaughlin, M. M. & Doolin, D. M. (2005). Influence of kinematics on landslide mobility and failure mode. *Journal of Geotechnical and Geoenvironmental Engineering* **131**, 716-728.

Sornette, D., Helmstetter, A., Andersen, J. V., Gluzman, S., Grasso, J. R. & Pisarenko, V. (2004). Towards landslide predictions: Two case studies. *Physica A: Statistical Mechanics and its Applications*, **338**, 605-632.

Superchi, L., Floris, M., Ghirotti, M., Genevois, R., Jaboyedoff, M. & Stead, D. (2010). Technical Note: Implementation of a geodatabase of published and unpublished data on the catastrophic Vaiont landslide. *Natural Hazards Earth System Science* **10**, 865-873.

Tika, T. E. & Hutchinson, J. N. (1999). Ring shear tests on soil from the Vaiont landslide slip surface. *Geotechnique* **49**, 59-74.

Utili, S. & Nova, R. (2008). DEM analysis of bonded granular geomaterials. *International Journal for Numerical and Analytical Methods in Geomechanics*, 32(17): 1997-2031.

Utili, S. & Crosta, G.B. (2011). Modelling the evolution of natural slopes subject to weathering: Part I. Limit analysis approach. *Journal of Geophysical Research – Earth Surface*, 116, F01016, doi:10.1029/2009JF001557.

Utili, S. & Crosta, G.B. (2011) Modelling the evolution of natural slopes subject to weathering: Part II. Discrete element approach *Journal of Geophysical Research – Earth Surface*, 116, F01017, doi:10.1029/2009JF001559.

Vardoulakis, I. (2002). Dynamic thermo-poro-mechanical analysis of catastrophic landslides. *Geotechnique* **52**, 157-171.

Veveakis, E., Vardoulakis, I. & Di Toro, G. (2007). Thermoporomechanics of creeping landslides: The 1963 Vaiont slide, northern Italy. *Journal of Geophysical Research - Earth Surface* **112**, F03026.

Voight, B. & Faust, C. (1982). Frictional heat and strength loss in some rapid landslides. *Geotechnique* **32**, 43-54.

Wolter, A., Stead, D. & Clague, J. J. (2014). A morphologic characterisation of the 1963 Vajont Slide, Italy, using long-range terrestrial photogrammetry. *Geomorphology* **206**, 147-164.

Table 1: Experimental data on the Vajont case study.

Authors	Test description	Slide surface friction angle (°)	Rock cohesion (MPa)	Rock friction angle (°)
Nonveiller (1967)	Crushed debris containing sand, clay or silt with angular fragments of limestone	N/A	0 - 0.098	22.4 - 42.5
	Clay material	5.6 - 6.8 (c= 0.00981 - 0.149 MPa)		
Hendron & Patton (1985)	Wet	6 - 10	N/A	N/A
Tika & Hutchinson (1999)	Wet, peak friction angle	30	N/A	N/A
	Wet, residual friction angle	9.7 - 10.6	N/A	N/A
	Wet, v > 0.075 m/s	4.4	N/A	N/A
Ferri et al. (2011)	Room humidity, $v < 5\times10^{-5}$ m/s	25.17	N/A	N/A
	Room humidity, v = 1.31 m/s	6.8	N/A	N/A
	Wet, $v < 5\times10^{-5}$ m/s	9.65	N/A	N/A
	Wet, v > 0.70 m/s	0	N/A	N/A

v = shear velocity

Table 2: Strength parameters adopted by investigators for calculations

Authors	Slide surface friction angle (°)	Rock cohesion (MPa)	Rock friction angle (°)	Purpose
Müller (1968, p. 43)	40.0 (clay absent)			Stability analysis
Chowdhury (1978)	28			Sensitivity analysis on horizontal stresses
Voight & Faust (1982)	13.28 (Model 1) 26.57 (Model 2-4)			Thermo-poro-mechanical analysis for velocity calculation
Hendron & Patton (1987)	12 (clay)	0	40 (Inter-slice) 30 (Inter-slice) 36 (East wall)	Stability analysis (Spencer method but satisfying only force equilibrium)
			30 (Inter-slice) 25 (East wall)	Dynamic analysis
Nonveiller (1987)	22.4			Thermo-poro-mechanical analysis for velocity calculation
Veveakis et al. (2007)	22.2 (peak) 10.2 (residual)			Thermo-poro-mechanical analysis for creep calculation
Alonso & Pinyol (2010)	12 12	0.55-1.25 0.787	38 - 40 38.5	Estimated of strength values
Pinyol & Alonso (2010)	12	0.762	38	Thermo-poro-mechanical analysis for velocity calculation

Table 3: Strength parameters obtained from back calculations.

Authors	Slide surface friction angle (°)	Interslice/ rock		Water level (m)	Type of calculation
		Cohesion (MPa)	Friction angle (°)		
Mencl (1966a)	18.75	0.49	30	700	Prandtl Wedge (2 inclined shear planes)
Mencl (1966b)	17.5	0	30	700	Prandtl Wedge different from Mencl (1966a)
Kenney (1967)	22.2			700	Janbu's generalised method
Nonveiller (1967)	17.6 20.6			700 700	Spencer Spencer (Assumed φ = 15° at the "seat")
Müller (1968)	22.5 21.9 20.8			700 700 Phreatic water table	Petterson Janbu's generalised method Spencer
Lo (1972)	25 13	0 0	25 13	Phreatic water table 700	Wedge analysis (Assumed φ = 28° at the "back")
Corbyn (1982)	18.43			700	Dynamic analysis
Nonveiller (1987)	22.4			700	Spencer
Vardoulakis (2002)	22.3			Phreatic water table	Taylor's friction circle method
Sitar et al. (2006)	8 - 14 (number of blocks = 2, with different joint orientation) 15 (number of blocks = 3-23) 16 (number of blocks = 105) 20	0	40 (static) 32 (dynamic)	0 0 0 Pore-pressure/overburden-pressure = 0.3	Discontinuous deformation analysis (DDA)
Crosta et al. (2007)	c=141.5-168.5kPa, φ=18.9-22.5° c=163.0-206. kPa, φ=16.3-20.7°	1.0	40 30	Different reservoir levels and different rainfall conditions	Finite element analysis *c*-*φ* strength reduction
Veveakis et al. (2007)	22.3			Phreatic water table	Limit analysis to calculate stresses Sliding block to calculate *φ* from stresses
Alonso & Pinyol (2010)	12 (assumed) 12 (assumed)	0.7623 0.564	38 40	710 710	Wedge analysis
Paronuzzi et al. (2013)	17.5 - 27	Not mentioned	Not mentioned	700	Finite element analyses

Table 4: Normal and shear stiffnesses used in the model for different mean joint spacings.

mean joint spacing (m)	normal stiffness (GPa/m)	shear stiffness (GPa/m)
300	0.0256	0.01024
150	0.0512	0.02048
120	0.064	0.0256
80	0.096	0.0384
60	0.128	0.0512
40	0.192	0.0768
30	0.256	0.1024
20	0.384	0.1536

Table 5: Properties of materials used in the ~~central~~ reference 2-D DEM analysis

Properties	Values
Slide surface normal stiffness	2 GPa/m
Slide surface shear stiffness	0.1 GPa/m
Rock joint spacing	40 m
Rock joint normal stiffness	0.192 GPa/m
Rock joint shear stiffness	0.0768 GPa/m
Rock joint friction angle (peak and residual)	40°
Rock joint cohesion (peak)	0.787 MPa
Rock joint cohesion (residual)	0 MPa
Rock joint tensile strength (peak)	0.076 MPa
Rock joint tensile strength (residual)	0 MPa
Unit weight (adopted from Alonso & Pinyol, 2010)	23.5 kN/m^3
Viscous damping ratio, ξ	0.1
Water table	90 m above horizontal slide surface

Table 6: Number of blocks in the numerical model generated from several mean spacings

mean joint spacing (m)	number of blocks	failure friction angle (°)
300	4	18.7
150	15	20.9
120	58	21.0
80	83	21.2
60	132	20.9
40	225	20.6
30	411	20.6
20	741	20.6

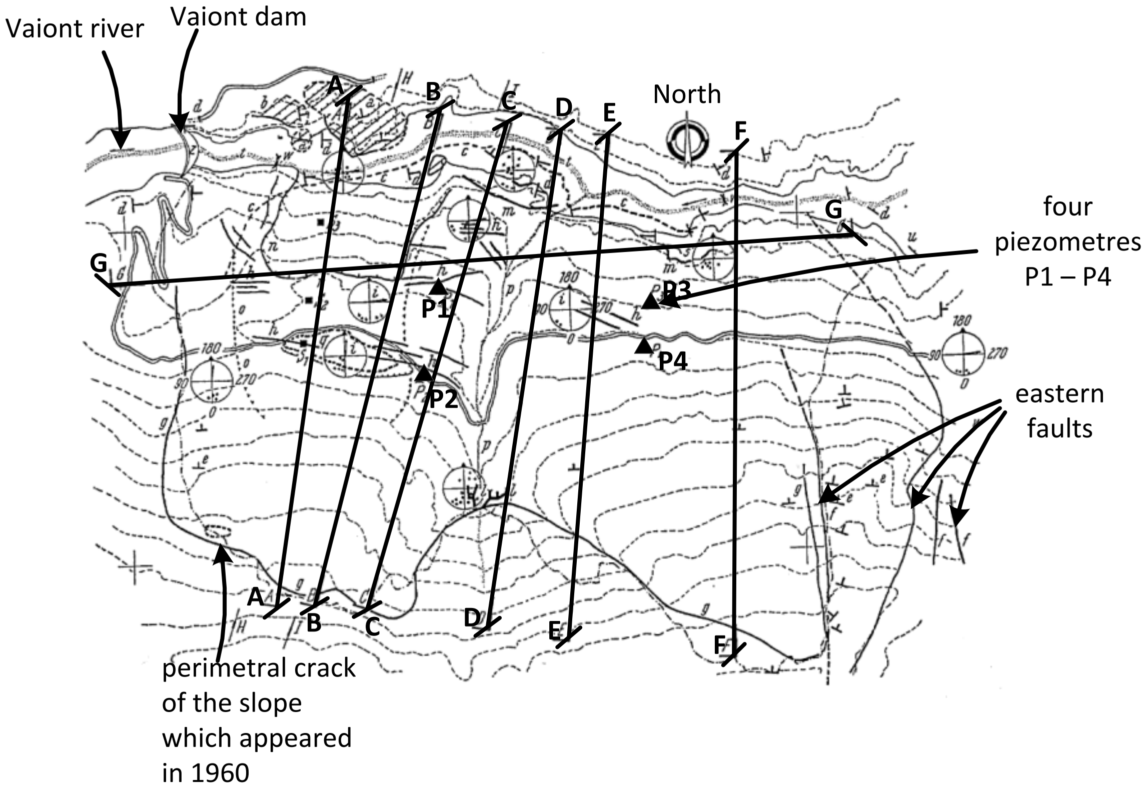

Fig. 1. Plan view of Vajont slope (modified after Fig. 5 in Broili, 1967).

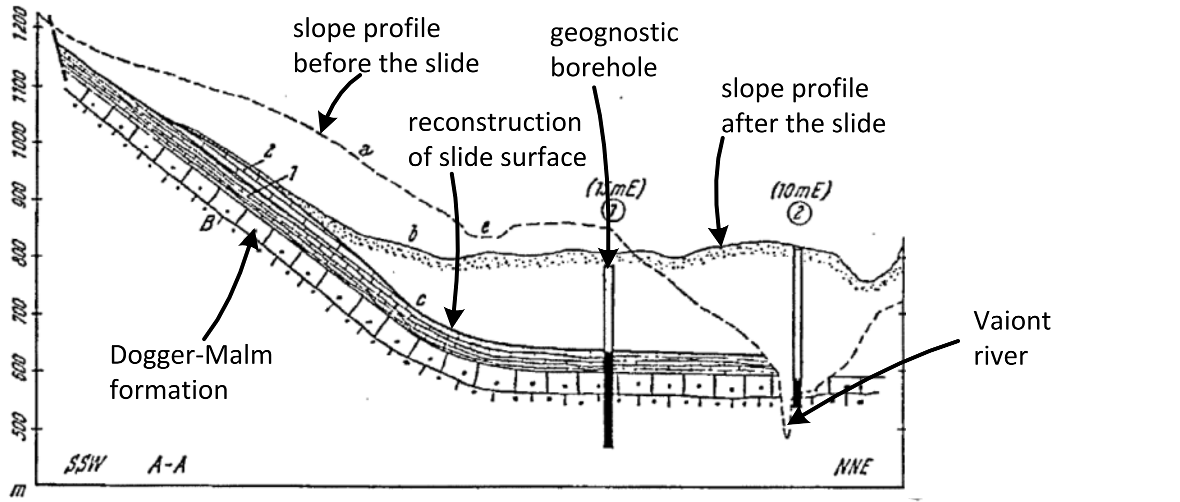

Fig. 2. Western end of slope, viewed from the East, section A-A of Fig. 1 (modified after Fig. 9 in Broili, 1967). For annotation see Fig. 3.

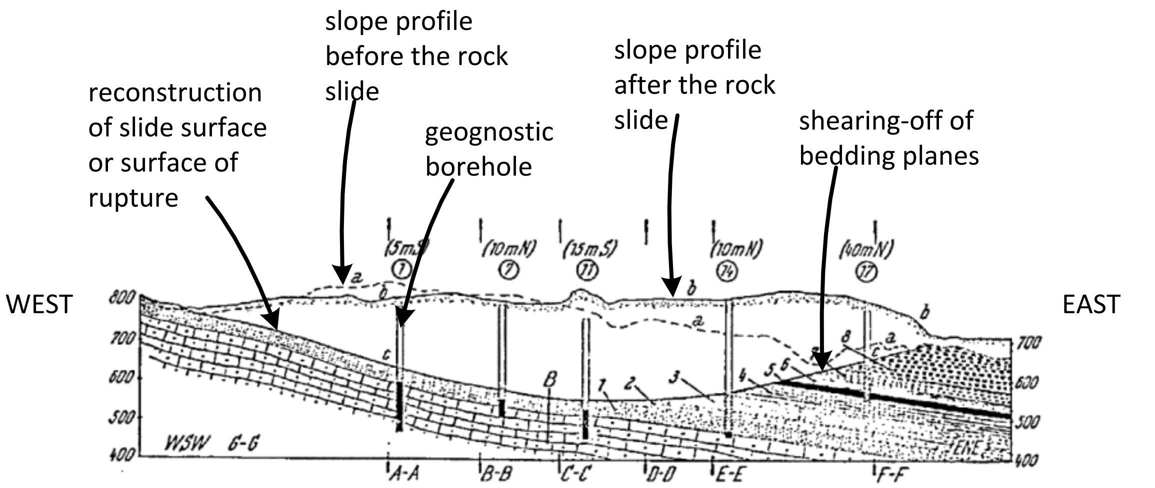

Fig. 3. West-East section of slide surface. Section G-G in Fig. 1 (modified after Fig. 11 in Broili, 1967). B - Oolitic limestone (not involved in the slide); 1 – grey limestone bearing nodules or beds of dark chert; 2 – compact limestone, often greyish or reddish with nodular structure; 3 – greyish to blue limestone bearing nodules or beds of chert, intercalated with marly limestone; 4 – greenish or pink limestone bearing nodules or beds of chert, intercalated with marly limestone; 5 – brecciated limestone, intercalated with marly limestone; 6 – greyish or pink, sometimes marly limestone; 7 – greyish and brecciated limestone bearing nodules or beds of chert; 8 – greyish and reddish limestone, bearing nodules of chert; a – topographic surface before the slide; b – topographic surface after the slide; c – reconstructed surface of rupture and sliding; e – depression of the “seat” area.

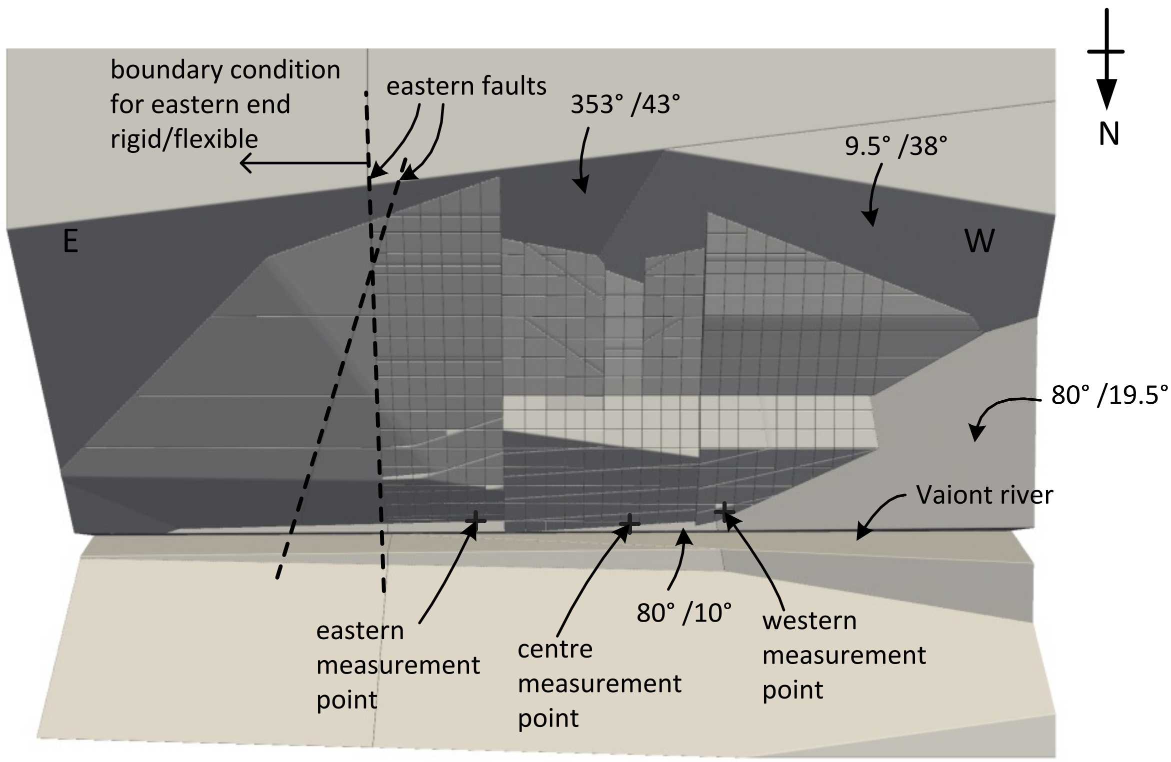

(a)

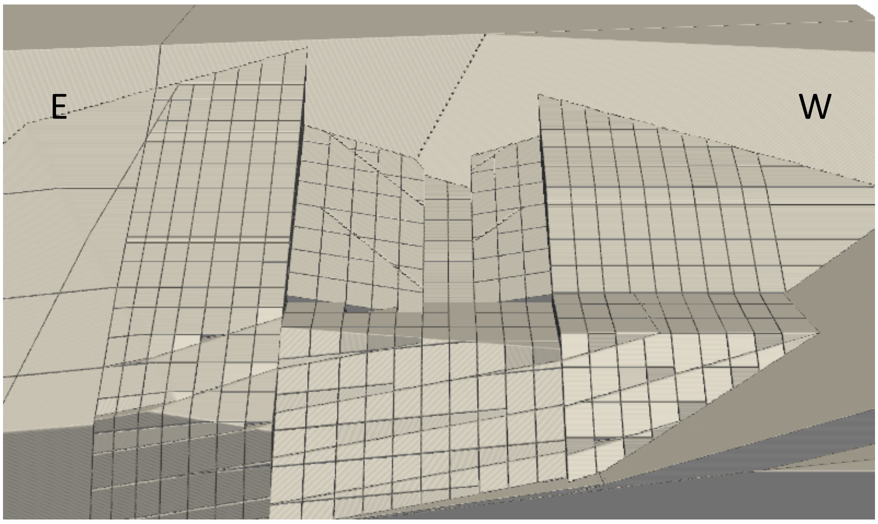

(b)

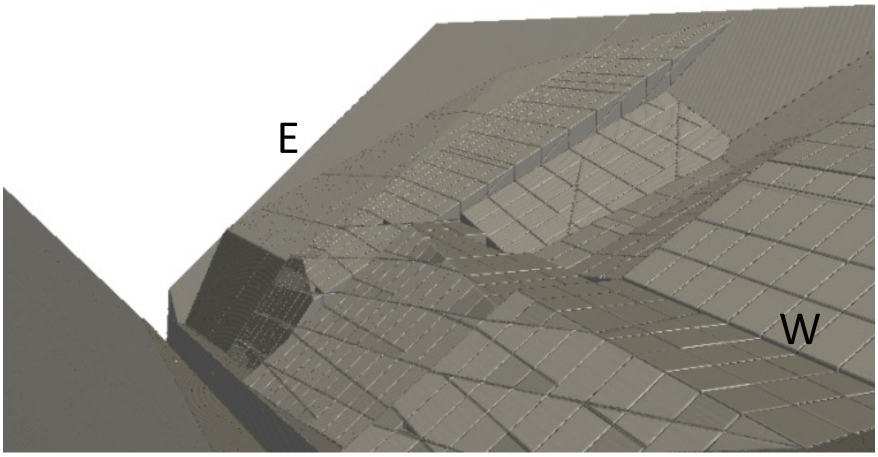

(c)

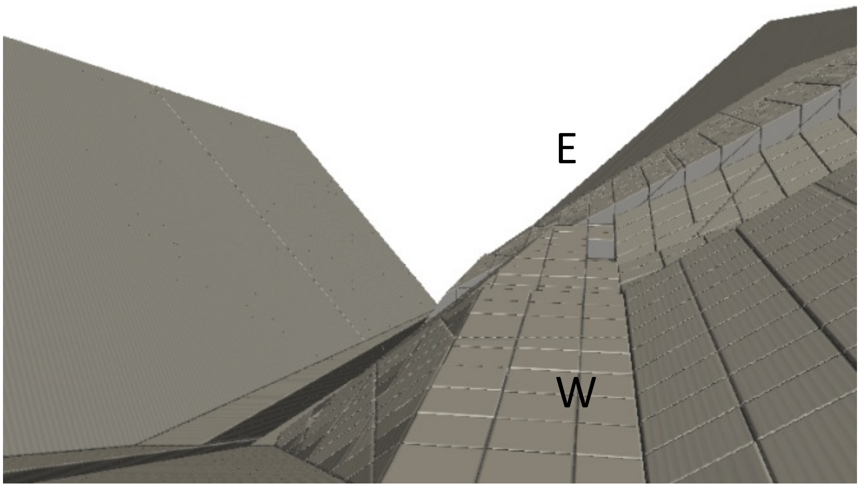

(d)

Fig. 4. Views of the slope: (a) plan view of slope mode, (b) view from front, (c) view from western end, (d) view from western end facing east along slope profile in 3-D model.

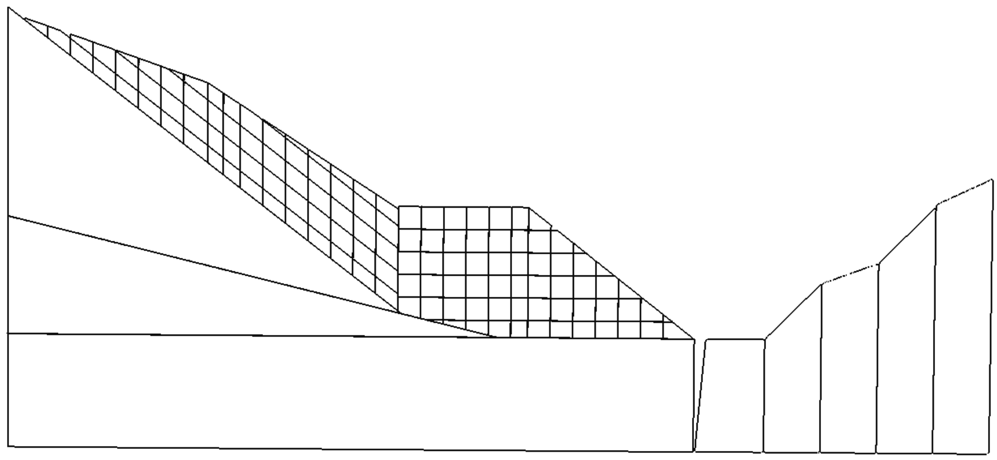

Fig. 5. Western end of slope, viewed from the East, section A-A

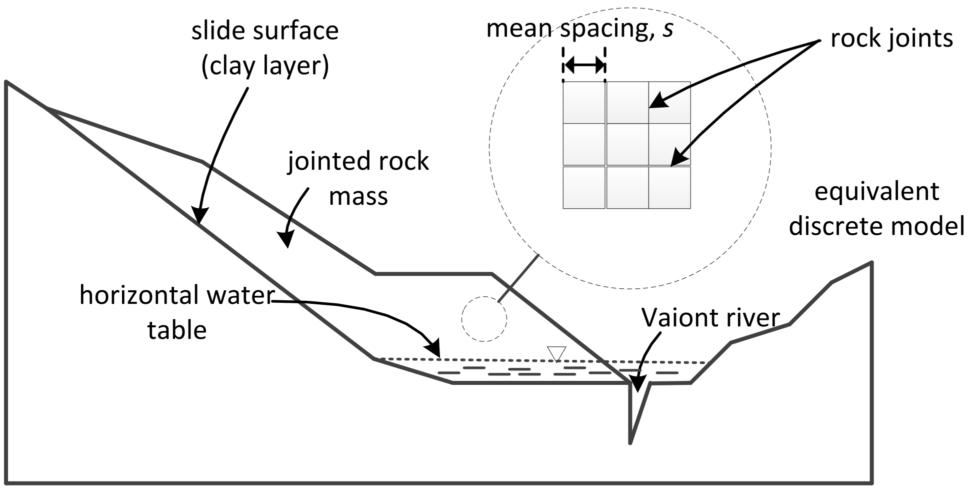

Fig. 6. Schematic diagram of the numerical model. Different stiffness and strength parameters are used for the slide surface and jointed rock mass.

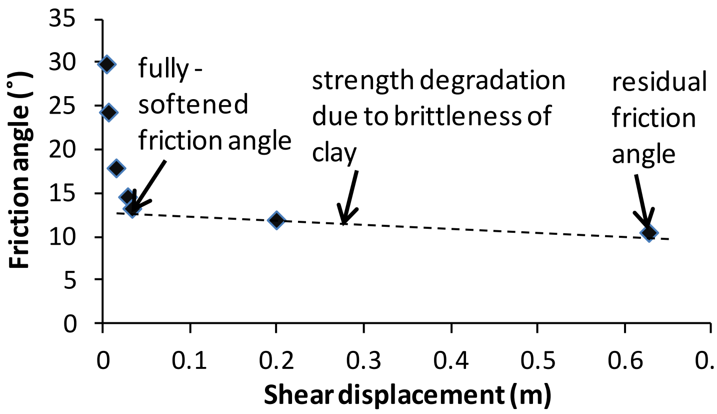

(a)

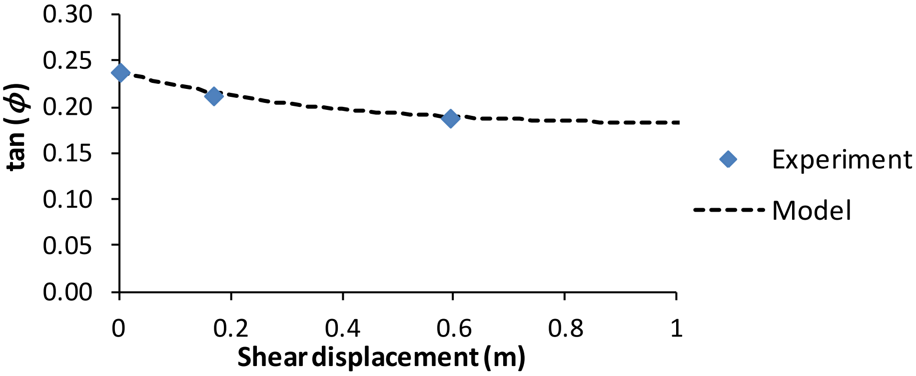

(b)

Fig. 7. Slide surface resistance: (a) ring shear tests on remoulded clay specimens retrieved from the slide surface (values adopted from Vardoulakis, 2002; originally by Tika & Hutchinson, 1999), (b) shear softening model (Eq. (6.7)) for clay layer at the slide surface, compared against experimental trend

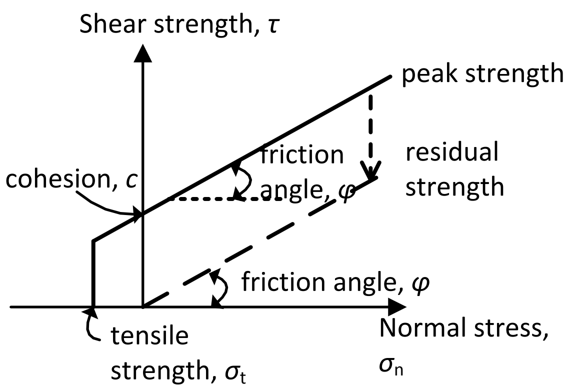

Fig. 8. Shear strength model for rock joints

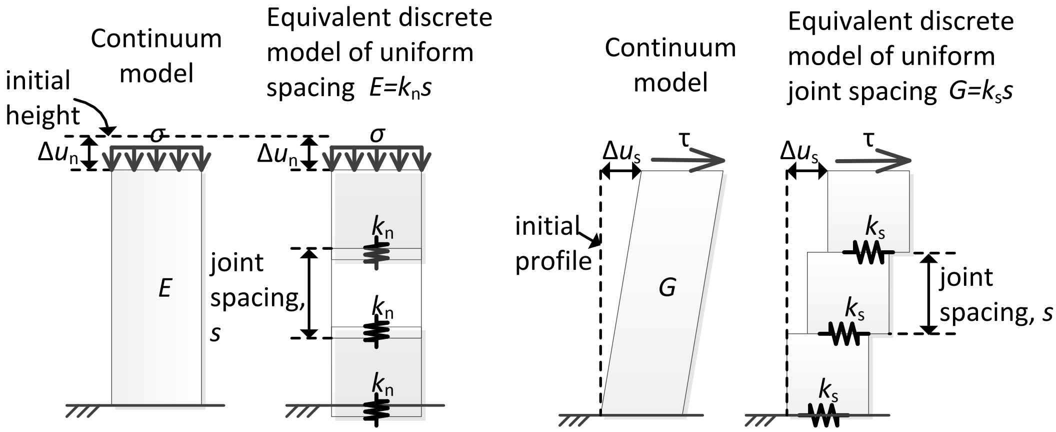

Fig. 9. Method to scale deformability of a continuum body using discrete bodies

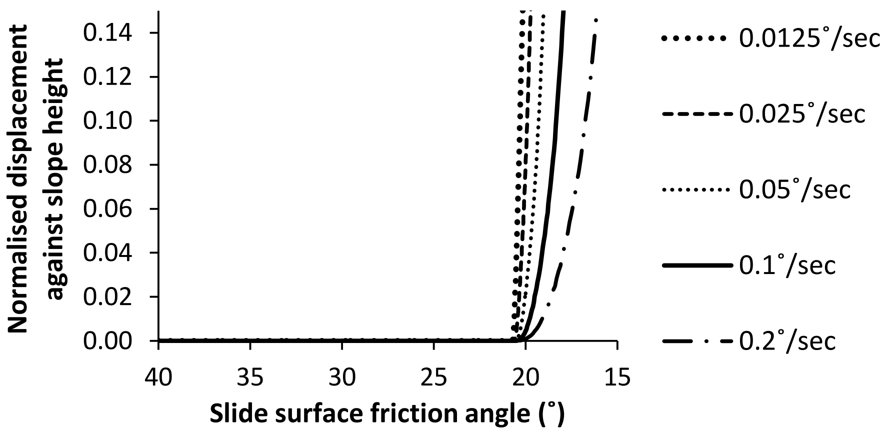

Fig. 10. Influence of strength reduction rate on the slope response.

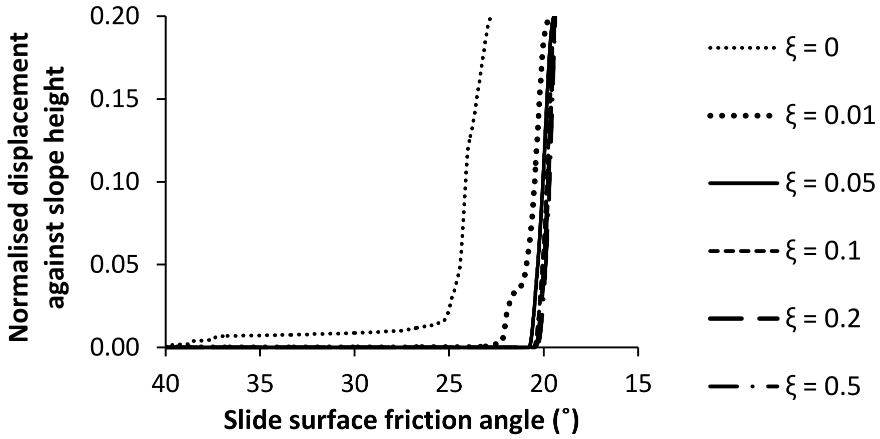

Fig. 11. Influence of viscous damping ratio on slope response.

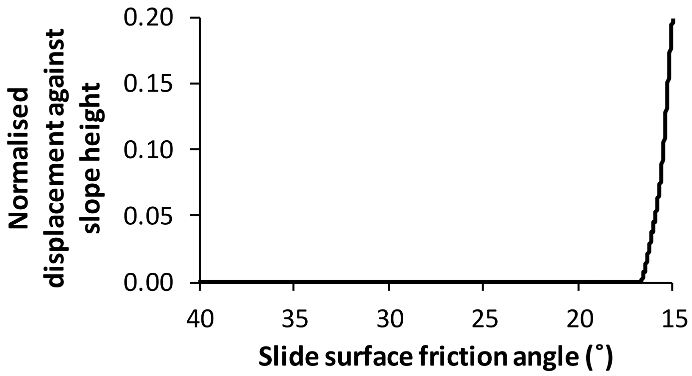

Fig. 12. Displacement with slide surface friction angle to compare with Sitar et al. (2005). Mean joint spacing: 40 m, viscous damping ratio ξ = 0.1

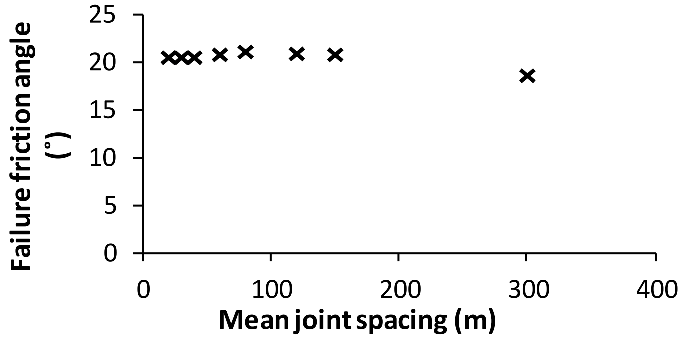

(a)

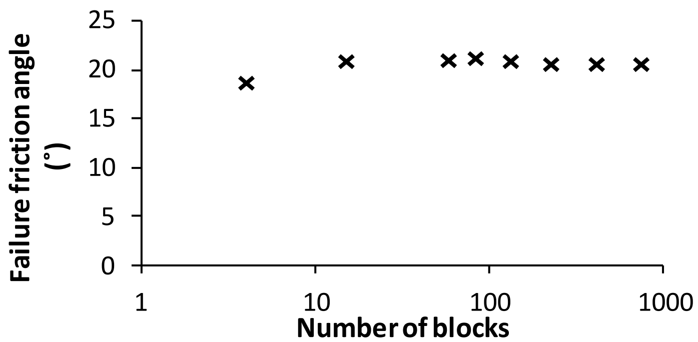

(b)

Fig. 13. Influence of (a) mean joint spacing and (b) the number of blocks on the friction angle required for stability (slide surface).

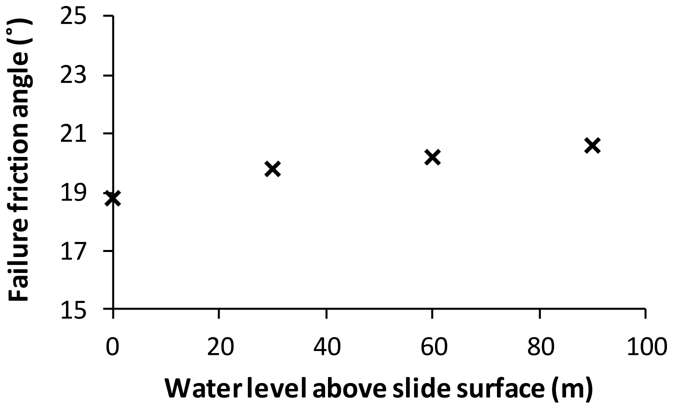

Fig. 14. Influence of water level on the friction angle required for stability (slide surface).

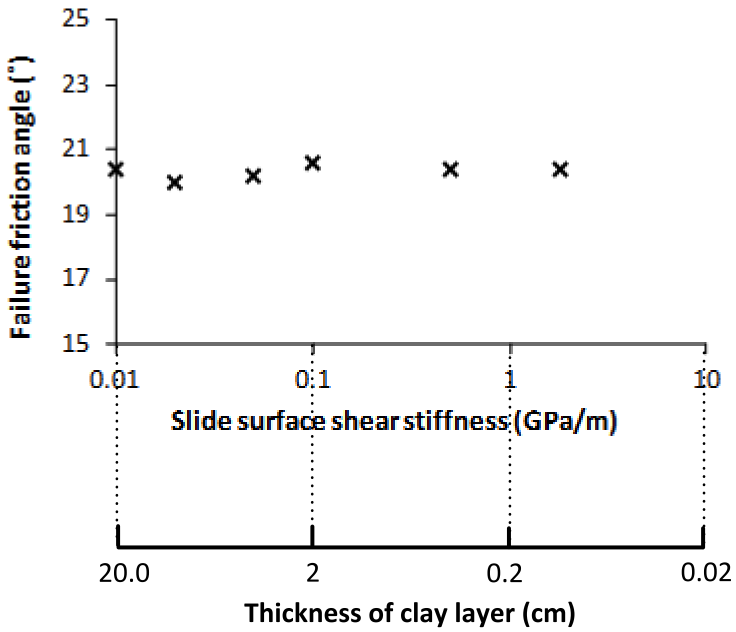

Fig. 15. Influence of slide surface shear stiffness on the friction angle required for stability (slide surface). The equivalent thickness of the clay layer for different shear stiffness values had been extrapolated from experimental shear tests reported by Ferri et al. (2011). Failure friction angle shows no clear dependence on slide surface shear stiffness.

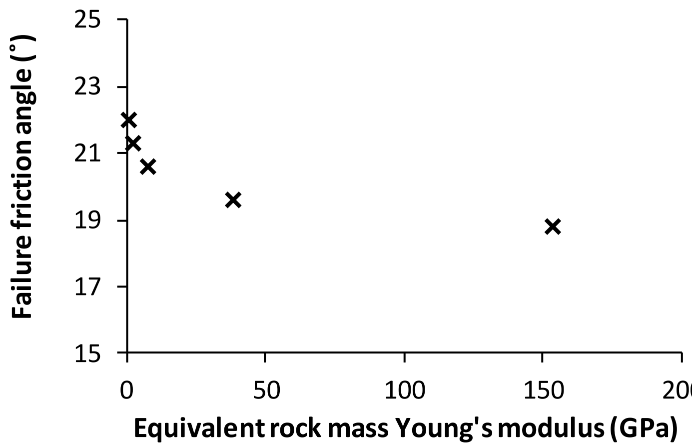

Fig. 16. Influence of equivalent rock mass deformability on the friction angle required for stability (slide surface). Refer to Eqs. (2) and (3) for the method of approximating the rock mass deformability.

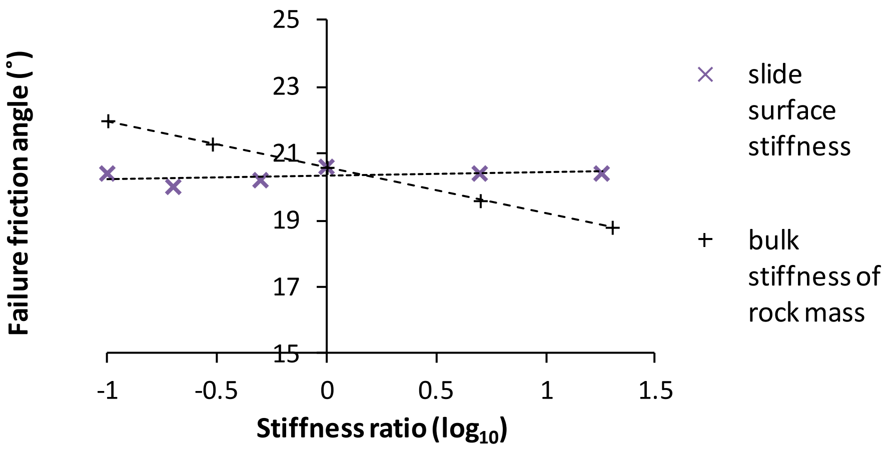

Fig. 17. Influence of rock mass and slide surface stiffness on the friction angle required for stability (slide surface).

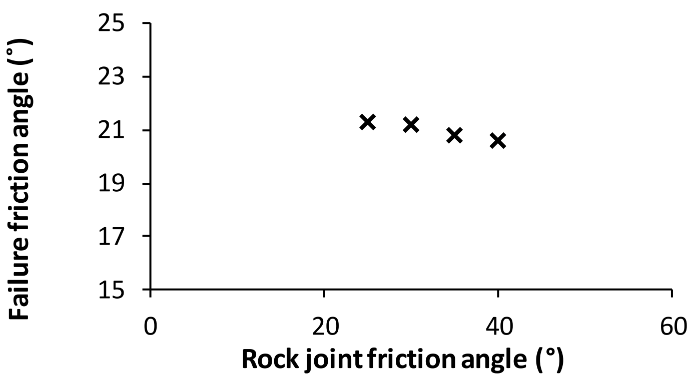

Fig. 18. Influence of rock joint friction angle on the friction angle required for stability (slide surface)

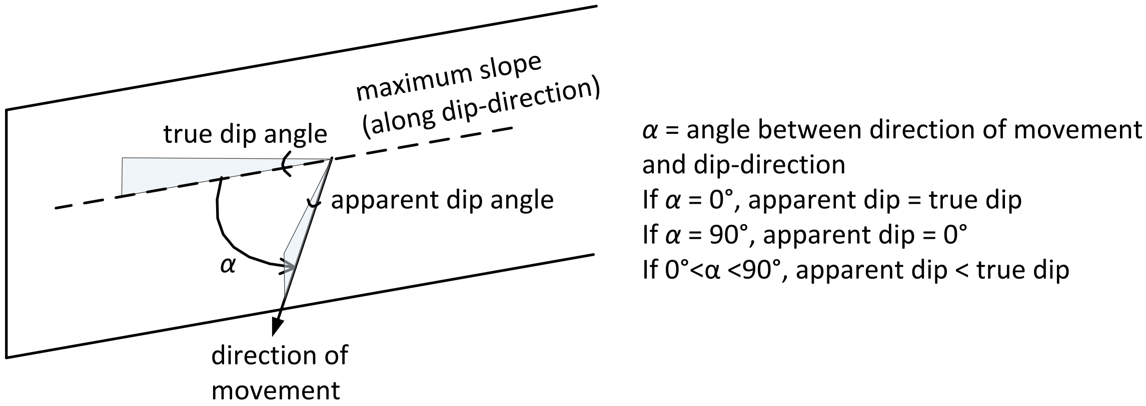

Fig. 19. Illustration of the influence of direction of movement and dip-direction on apparent dip angle.

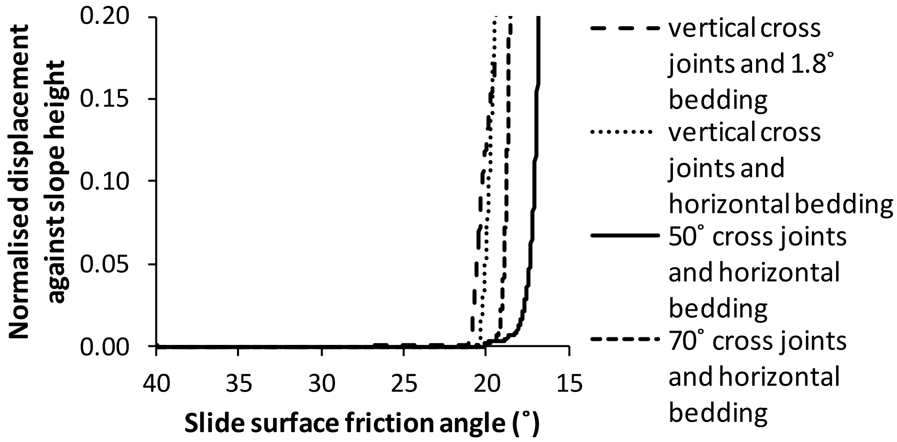

Fig. 20. Influence of rock joint orientation on the critical sliding friction angle.

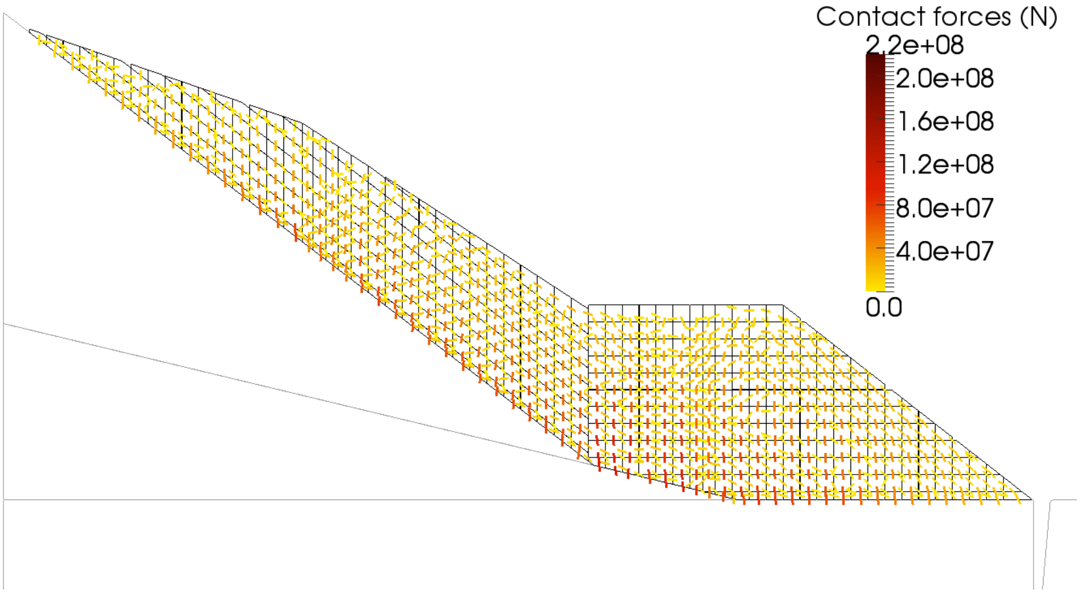
Contact forces (N)
2.2e+08
2.0e+08
1.6e+08
1.2e+08
8.0e+07
4.0e+07
0.0

(a)

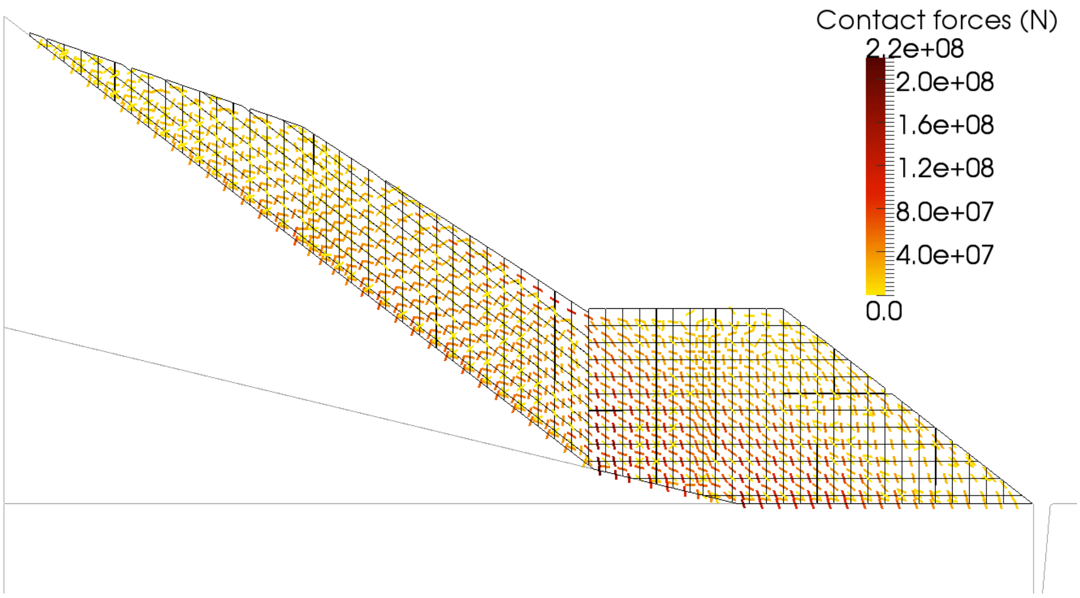
Contact forces (N)
2.2e+08
2.0e+08
1.6e+08
1.2e+08
8.0e+07
4.0e+07
0.0

(b)

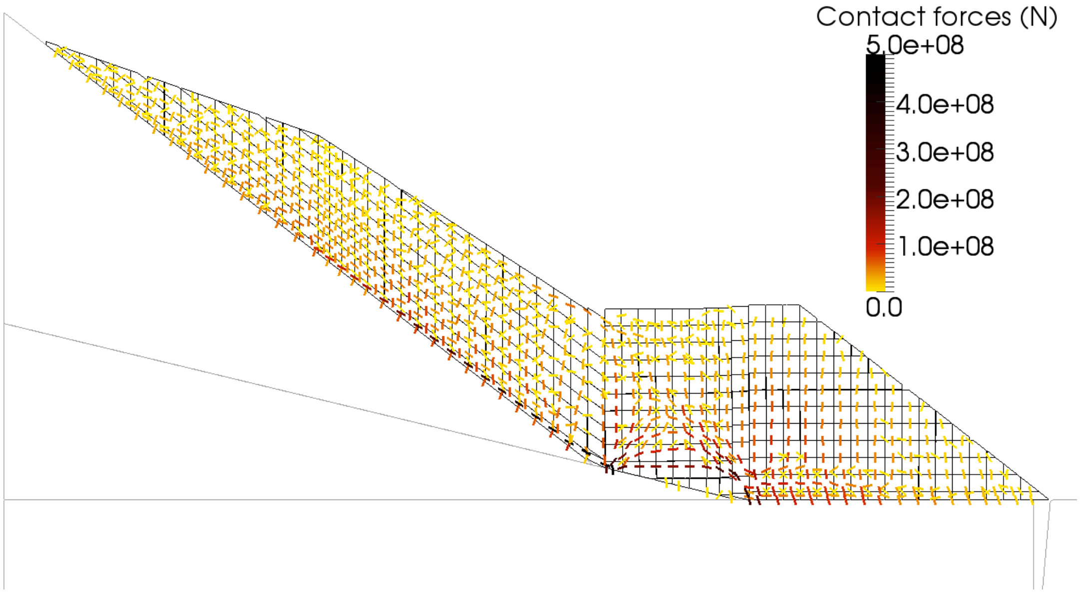

(c)

Fig. 21. Contact forces when (a) slide surface friction angle = 35.65°, (b) slide surface friction angle = 20.65° (before failure) (c) slide surface friction angle = 20.23° (after failure), displacement 20 m. Mean joint spacing = 20 m, 40° rock joint friction angle.

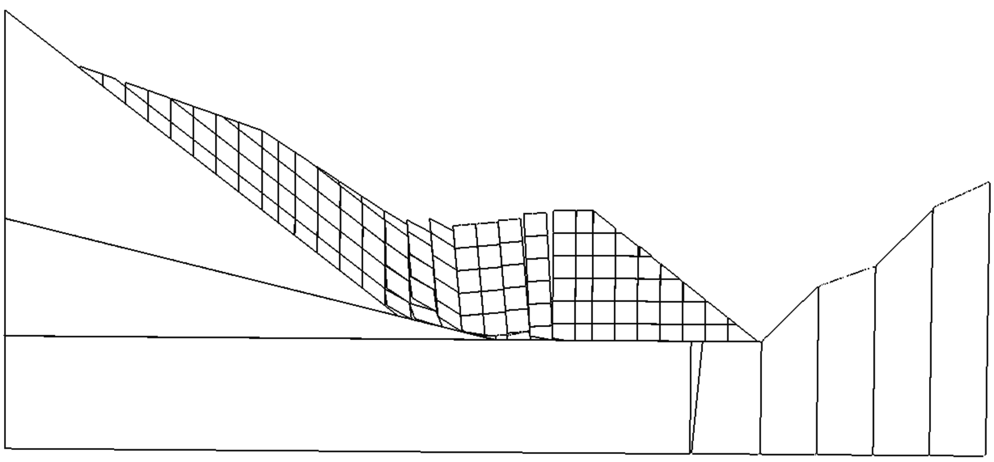

(a)

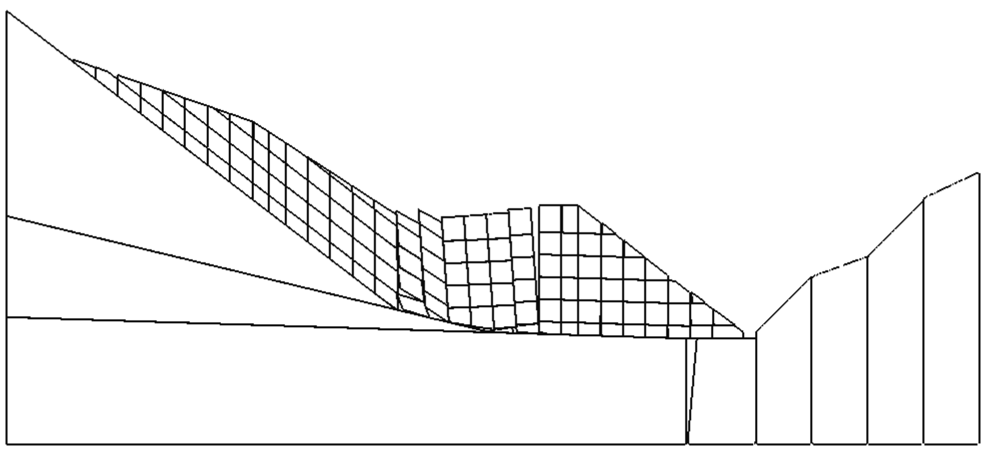

(b)

(c)

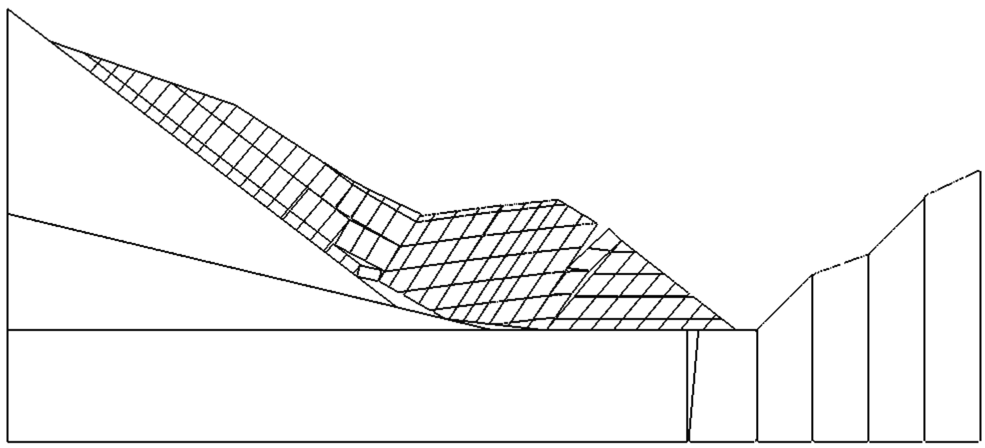

(d)

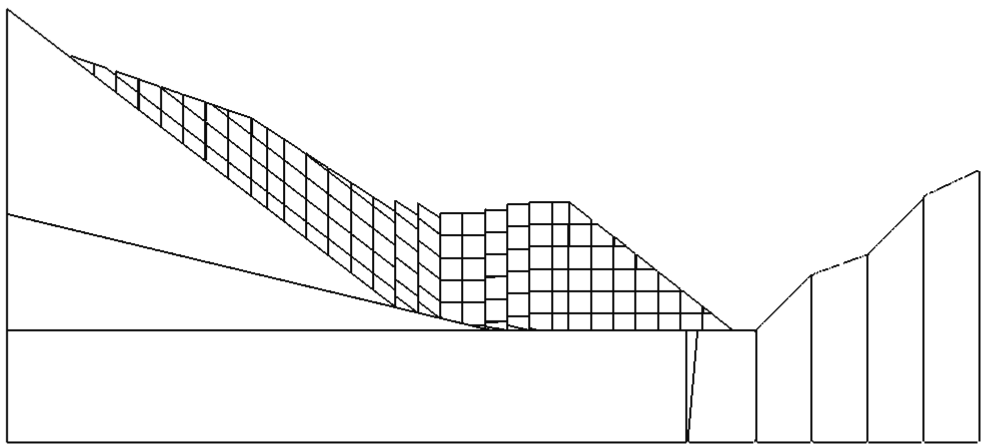

Fig. 22. Failure mechanism for (a) vertical cross-joints (ϕ_{joint} = 40°) (b) inclined sub-horizontal joints and seat of slide surface, dip angle = 1.8° (ϕ_{joint} = 40°) (c) inclined cross-joints, dip angle = 50° South (ϕ_{joint} = 40°), (d) vertical cross-joints (ϕ_{joint} = 30°).

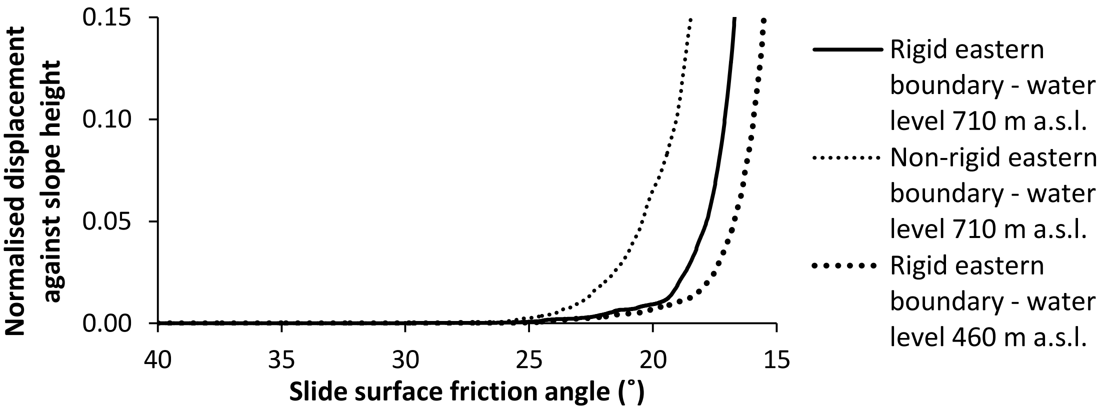

Fig. 23. Influence of eastern boundary and water level on the critical friction angle

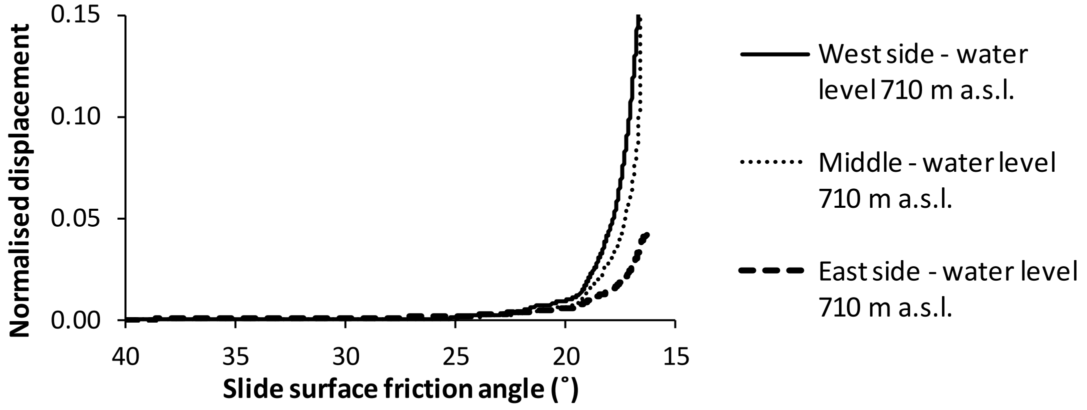

(a)

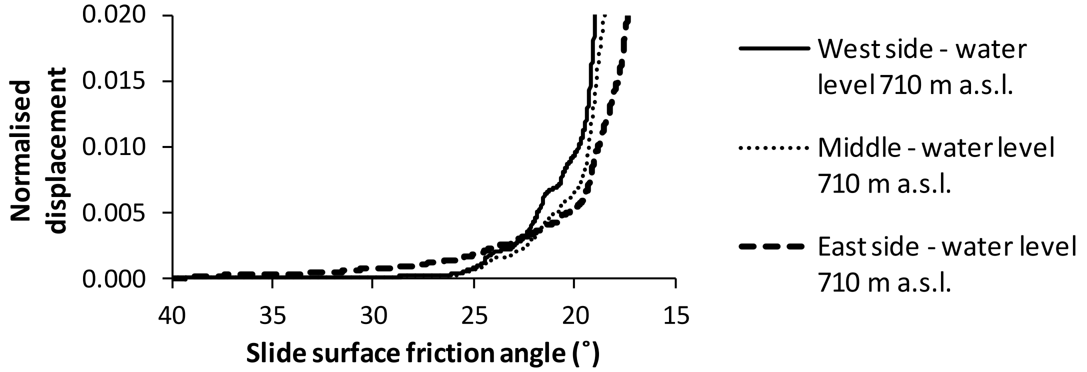

(b)

Fig. 24. Displacement of different parts of the slope (rigid eastern boundaries) with strength reduction: (a) and (b) are drawn using different scales in the vertical axes. Measurement points are annotated in Fig. 4 (a).

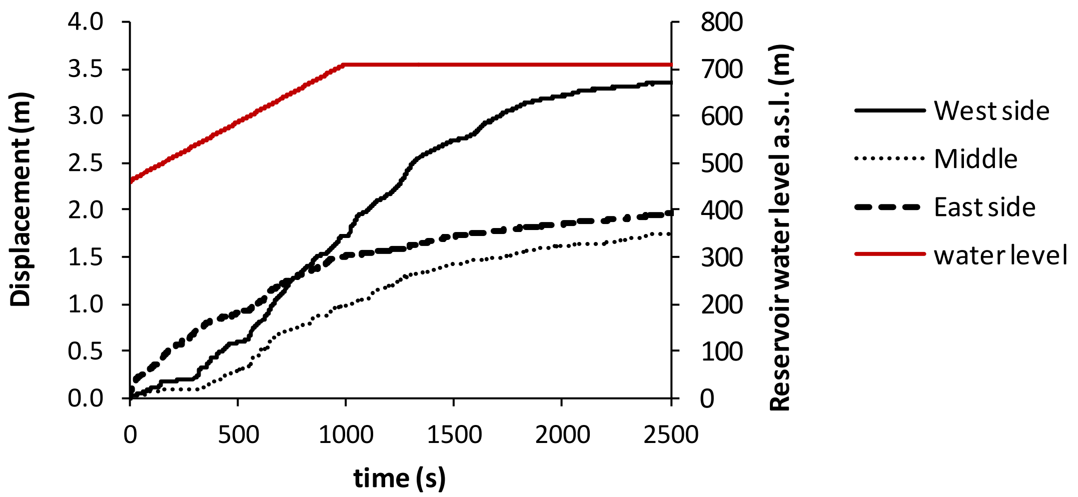

(a)

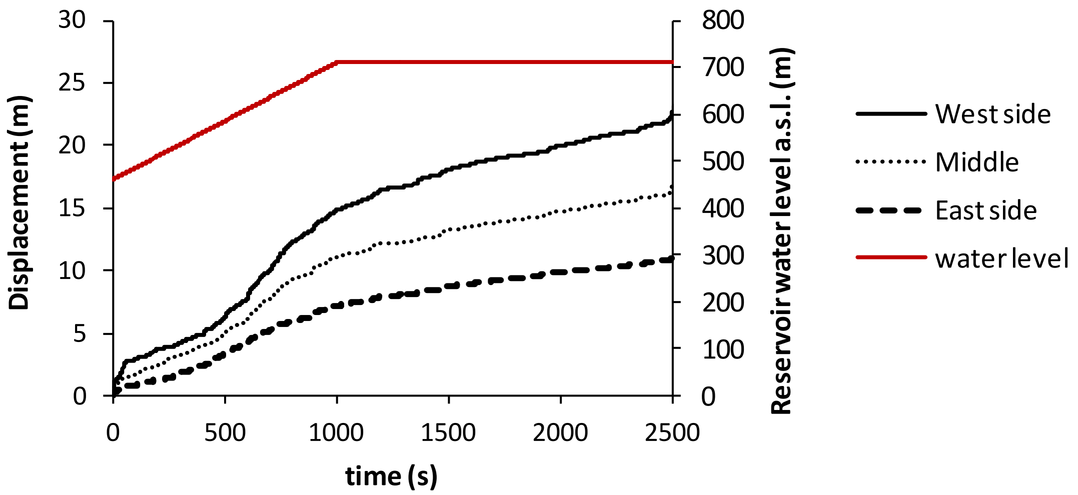

(b)

Fig. 25. Slope movement with reservoir filling at slide surface friction angles (a) 26° and (b) 21°. Measurement points are annotated in Fig. 4 (a).

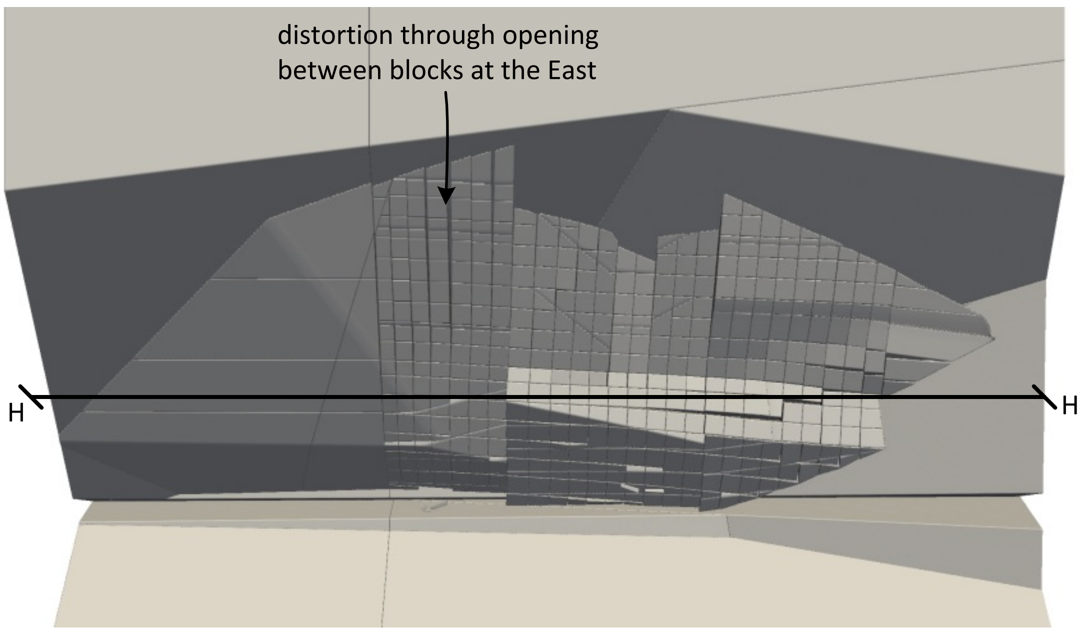

(a)

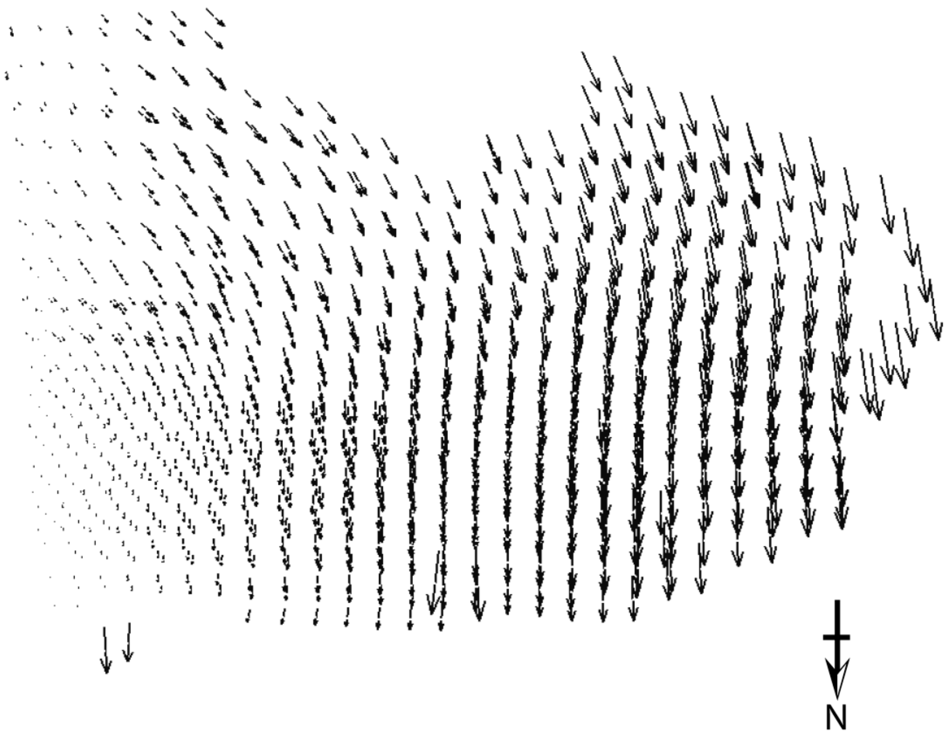

(b)

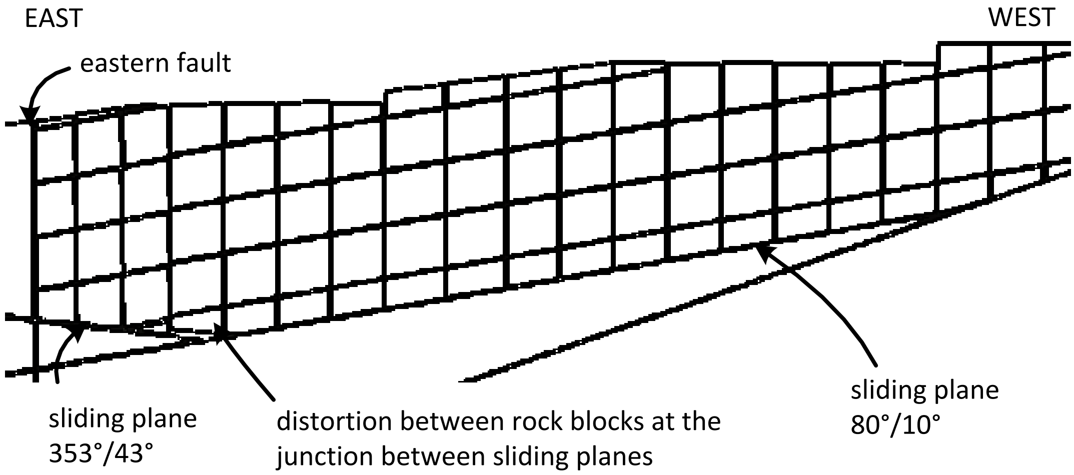

(c)

Fig. 26. View of failed slope: (a) plan view, (b) displacement vectors from original positions, (c) H-H' section (jagged lines are numerical artifacts of the display tool).